Preprint typeset in JINST style - HYPER VERSION

Alignment of the ALICE Inner Tracking System with cosmic-ray tracks

ALICE collaboration

ABSTRACT: ALICE (A Large Ion Collider Experiment) is the LHC (Large Hadron Collider) experiment devoted to investigating the strongly interacting matter created in nucleus-nucleus collisions at the LHC energies. The ALICE ITS, Inner Tracking System, consists of six cylindrical layers of silicon detectors with three different technologies; in the outward direction: two layers of pixel detectors, two layers each of drift, and strip detectors. The number of parameters to be determined in the spatial alignment of the 2198 sensor modules of the ITS is about 13,000. The target alignment precision is well below 10 μm in some cases (pixels). The sources of alignment information include survey measurements, and the reconstructed tracks from cosmic rays and from proton–proton collisions. The main track-based alignment method uses the Millepede global approach. An iterative local method was developed and used as well. We present the results obtained for the ITS alignment using about 10^5 charged tracks from cosmic rays that have been collected during summer 2008, with the ALICE solenoidal magnet switched off.

KEYWORDS: Particle tracking detectors (Solid-state detectors); Detector alignment and calibration methods.

Contents

ALICE collaboration

K. Aamodt[78], N. Abel[43], U. Abeysekara[30], A. Abrahantes Quintana[42], D. Adamová[86], M.M. Aggarwal[25], G. Aglieri Rinella[40], A.G. Agocs[18], S. Aguilar Salazar[66], Z. Ahammed[55], A. Ahmad[2], N. Ahmad[2], S.U. Ahn[50 i], R. Akimoto[100], A. Akindinov[68], D. Aleksandrov[70], B. Alessandro[102], R. Alfaro Molina[66], A. Alici[13], E. Almaráz Aviña[66], J. Alme[8], T. Alt[43 ii], V. Altini[5], S. Altinpinar[32], C. Andrei[17], A. Andronic[32], G. Anelli[40], V. Angelov[43 ii], C. Anson[27], T. Antičić[113], F. Antinori[40 iii], S. Antinori[13], K. Antipin[37], D. Antończyk[37], P. Antonioli[14], A. Anzo[66], L. Aphecetche[73], H. Appelshäuser[37], S. Arcelli[13], R. Arceo[66], A. Arend[37], N. Armesto[92], R. Arnaldi[102], T. Aronsson[74], I.C. Arsene[78 iv], A. Asryan[98], A. Augustinus[40], R. Averbeck[32], T.C. Awes[76], J. Äystö[49], M.D. Azmi[2], S. Bablok[8],

M. Bach[36], A. Badalà[24], Y.W. Baek[50 i], S. Bagnasco[102], R. Bailhache[32 v], R. Bala[101], A. Baldisseri[89], A. Baldit[26], J. Bán[58], R. Barbera[23], G.G. Barnaföldi[18], L. Barnby[12], V. Barret[26], J. Bartke[29], F. Barile[5], M. Basile[13], V. Basmanov[94], N. Bastid[26], B. Bathen[72], G. Batigne[73], B. Batyunya[35], C. Baumann[72 v], I.G. Bearden[28], B. Becker[20 vi], I. Belikov[99], R. Bellwied[34], E. Belmont-Moreno[66], A. Belogianni[4], L. Benhabib[73], S. Beole[101], I. Berceanu[17], A. Bercuci[32 vii], E. Berdermann[32], Y. Berdnikov[39], L. Betev[40], A. Bhasin[48], A.K. Bhati[25], L. Bianchi[101], N. Bianchi[38], C. Bianchin[79], J. Bielčík[81], J. Bielčíková[86], A. Bilandzic[3], L. Bimbot[77], E. Biolcati[101], A. Blanc[26], F. Blanco[23 viii], F. Blanco[63], D. Blau[70], C. Blume[37], M. Boccioli[40], N. Bock[27], A. Bogdanov[69], H. Bøggild[28], M. Bogolyubsky[83], J. Bohm[96], L. Boldizsár[18], M. Bombara[12 ix], C. Bombonati[79 x], M. Bondila[49], H. Borel[89], V. Borshchov[51], A. Borisov[52], C. Bortolin[79 xl],, S. Bose[54], L. Bosisio[103], F. Bossú[101], M. Botje[3], S. Böttger[43], G. Bourdaud[73], B. Boyer[77], M. Braun[98], P. Braun-Munzinger[32,33 ii], L. Bravina[78], M. Bregant[103 xi], T. Breitner[43], G. Bruckner[40], R. Brun[40], E. Bruna[74], G.E. Bruno[5], D. Budnikov[94], H. Buesching[37], P. Buncic[40], O. Busch[44], Z. Buthelezi[22], D. Caffarri[79], X. Cai[111], H. Caines[74], E. Camacho[64], P. Camerini[103], M. Campbell[40], V. Canoa Roman[40], G.P. Capitani[38], G. Cara Romeo[14], F. Carena[40], W. Carena[40], F. Carminati[40], A. Casanova Díaz[38], M. Caselle[40], J. Castillo Castellanos[89], J.F. Castillo Hernandez[32], V. Catanescu[17], E. Cattaruzza[103], C. Cavicchioli[40], P. Cerello[102], V. Chambert[77], B. Chang[96], S. Chapeland[40], A. Charpy[77], J.L. Charvet[89], S. Chattopadhyay[54], S. Chattopadhyay[55], M. Cherney[30], C. Cheshkov[40], B. Cheynis[62], E. Chiavassa[101], V. Chibante Barroso[40], D.D. Chinellato[21], P. Chochula[40], K. Choi[85], M. Chojnacki[106], P. Christakoglou[106], C.H. Christensen[28], P. Christiansen[61], T. Chujo[105], F. Chuman[45], C. Cicalo[20], L. Cifarelli[13], F. Cindolo[14], J. Cleymans[22], O. Cobanoglu[101], J.-P. Coffin[99], S. Coli[102], A. Colla[40], G. Conesa Balbastre[38], Z. Conesa del Valle[73 xii], E.S. Conner[110], P. Constantin[44], G. Contin[103 x], G.J. Contreras[64], Y. Corrales Morales[101], T.M. Cormier[34], P. Cortese[1], I. Cortés Maldonado[84], M.R. Cosentino[21], F. Costa[40], M.E. Cotallo[63], E. Crescio[64], P. Crochet[26], E. Cuautle[65], L. Cunqueiro[38], J. Cussonneau[73], A. Dainese[59 iii], H.H. Dalsgaard[28], A. Danu[16], I. Das[54], S. Das[54], A. Dash[11], S. Dash[11], G.O.V. de Barros[93], A. De Caro[90], G. de Cataldo[6] J. de Cuveland[43 ii], A. De Falco[19], M. De Gaspari[44], J. de Groot[40], D. De Gruttola[90], A.P. de Haas[106] N. De Marco[102], S. De Pasquale[90], R. De Remigis[102], R. de Rooij[106], G. de Vaux[22], H. Delagrange[73], G. Dellacasa[1], A. Deloff[107], V. Demanov[94], E. Dénes[18], A. Deppman[93], G. D'Erasmo[5], D. Derkach[98], A. Devaux[26], D. Di Bari[5], C. Di Giglio[5 x], S. Di Liberto[88], A. Di Mauro[40], P. Di Nezza[38], M. Dialinas[73], L. Díaz[65], R. Díaz[49], T. Dietel[72], H. Ding[111], R. Divià[40], Ø. Djuvsland[8], V. Dobretsov[70], A. Dobrin[61], T. Dobrowolski[107], B. Dönigus[32], I. Domínguez[65], D.M.M. Don[46] O. Dordic[78], A.K. Dubey[55], J. Dubuisson[40], L. Ducroux[62], P. Dupieux[26], A.K. Dutta Majumdar[54], M.R. Dutta Majumdar[55], D. Elia[6], D. Emschermann[44 xiv], A. Enokizono[76], B. Espagnon[77], M. Estienne[73], D. Evans[12], S. Evrard[40], G. Eyyubova[78], C.W. Fabjan[40 xv], D. Fabris[79], J. Faivre[41], D. Falchieri[13], A. Fantoni[38], M. Fasel[32], O. Fateev[35], R. Fearick[22], A. Fedunov[35], D. Fehlker[8], V. Fekete[15], D. Felea[16], B. Fenton-Olsen[28 xvi], G. Feofilov[98], A. Fernández Téllez[84], E.G. Ferreiro[92], A. Ferretti[101], R. Ferretti[1 xvii], M.A.S. Figueredo[93], S. Filchagin[94], R. Fini[6], F.M. Fionda[5], E.M. Fiore[5], M. Floris[19 x], Z. Fodor[18], S. Foertsch[22], P. Foka[32], S. Fokin[70], F. Formenti[40], E. Fragiacomo[104], M. Fragkiadakis[4], U. Frankenfeld[32], A. Frolov[75], U. Fuchs[40], F. Furano[40], C. Furget[41], M. Fusco Girard[90], J.J. Gaardhøje[28], S. Gadrat[41], M. Gagliardi[101], A. Gago[64 xviii], M. Gallio[101], S. Gang[111], P. Ganoti[4], M.S. Ganti[55], C. Garabatos[32], C. García Trapaga[101], J. Gebelein[43], R. Gemme[1], M. Germain[73], A. Gheata[40], M. Gheata[40], B. Ghidini[5], P. Ghosh[55], G. Giraudo[102], P. Giubellino[102], E. Gladysz-Dziadus[29], R. Glasow[72 xix], P. Glässel[44], A. Glenn[60], R. Gomez[31], H. González Santos[84], L.H. González-Trueba[66], P. González-Zamora[63],

S. Gorbunov[43 ii], Y. Gorbunov[30], S. Gotovac[97], H. Gottschlag[72], V. Grabski[66], R. Grajcarek[44], A. Grelli[106], A. Grigoras[40], C. Grigoras[40], V. Grigoriev[69], A. Grigoryan[112], S. Grigoryan[35], B. Grinyov[52], N. Grion[104], P. Gros[61], J.F. Grosse-Oetringhaus[40], J.-Y. Grossiord[62], R. Grosso[80], C. Guarnaccia[90], F. Guber[67], R. Guernane[41], B. Guerzoni[13], K. Gulbrandsen[28], H. Gulkanyan[112], T. Gunji[100], A. Gupta[48], R. Gupta[48], H.-A. Gustafsson[61], H. Gutbrod[32], Ø. Haaland[8], C. Hadjidakis[77], M. Haiduc[16], H. Hamagaki[100], G. Hamar[18], J. Hamblen[53], B.H. Han[95], J.W. Harris[74], M. Hartig[37], A. Harutyunyan[112], D. Hasch[38], D. Hasegan[16], D. Hatzifotiadou[14], A. Hayrapetyan[112], M. Heide[72], M. Heinz[74], H. Helstrup[9], A. Herghelegiu[17], C. Hernández[32], G. Herrera Corral[64], N. Herrmann[44], K.F. Hetland[9], B. Hicks[74], A. Hiei[45], P.T. Hille[78 xx], B. Hippolyte[99], T. Horaguchi[45 xxi], Y. Hori[100], P. Hristov[40], I. Hřivnáčová[77], S. Hu[7], M. Huang[8], S. Huber[32], T.J. Humanic[27], D. Hutter[36], D.S. Hwang[95], R. Ichou[73], R. Ilkaev[94], I. Ilkiv[107], M. Inaba[105], P.G. Innocenti[40], M. Ippolitov[70], M. Irfan[2], C. Ivan[106], A. Ivanov[98], M. Ivanov[32], V. Ivanov[39], T. Iwasaki[45], A. Jachołkowski[40], P. Jacobs[10], L. Jančurová[35], S. Jangal[99], R. Janik[15], C. Jena[11], S. Jena[71], L. Jirden[40], G.T. Jones[12], P.G. Jones[12], P. Jovanović[12], H. Jung[50], W. Jung[50], A. Jusko[12], A.B. Kaidalov[68], S. Kalcher[43 ii], P. Kaliňák[58], T. Kalliokoski[49], A. Kalweit[33], A. Kamal[2], R. Kamermans[106], K. Kanaki[8], E. Kang[50], J.H. Kang[96], J. Kapitan[86], V. Kaplin[69], S. Kapusta[40], O. Karavichev[67], T. Karavicheva[67], E. Karpechev[67], A. Kazantsev[70], U. Kebschull[43], R. Keidel[110], M.M. Khan[2], S.A. Khan[55], A. Khanzadeev[39], Y. Kharlov[83], D. Kikola[108], B. Kileng[9], D.J Kim[49], D.S. Kim[50], D.W. Kim[50], H.N. Kim[50], J. Kim[83], J.H. Kim[95], J.S. Kim[50], M. Kim[50], M. Kim[96], S.H. Kim[50], S. Kim[95], Y. Kim[96], S. Kirsch[40], I. Kisel[43 iv], S. Kiselev[68], A. Kisiel[27 x], J.L. Klay[91], J. Klein[44], C. Klein-Bösing[40 xiv], M. Kliemant[37], A. Klovning[8], A. Kluge[40], S. Kniege[37], K. Koch[44], R. Kolevatov[78], A. Kolojvari[98], V. Kondratiev[98], N. Kondratyeva[69], A. Konevskih[67], E. Kornaś[29], R. Kour[12], M. Kowalski[29], S. Kox[41], K. Kozlov[70], J. Kral[81 xi], I. Králik[58], F. Kramer[37], I. Kraus[33 iv], A. Kravčáková[57], T. Krawutschke[56], M. Krivda[12], D. Krumbhorn[44], M. Krus[81], E. Kryshen[39], M. Krzewicki[3], Y. Kucheriaev[70], C. Kuhn[99], P.G. Kuijer[3], L. Kumar[25], N. Kumar[25], R. Kupczak[108], P. Kurashvili[107], A. Kurepin[67], A.N. Kurepin[67], A. Kuryakin[94], S. Kushpil[86], V. Kushpil[86], M. Kutouski[35], H. Kvaerno[78], M.J. Kweon[44], Y. Kwon[96], P. La Rocca[23 xxii], F. Lackner[40], P. Ladrón de Guevara[63], V. Lafage[77], C. Lal[48], C. Lara[43], D.T. Larsen[8], G. Laurenti[14], C. Lazzeroni[12], Y. Le Bornec[77], N. Le Bris[73], H. Lee[85], K.S. Lee[50], S.C. Lee[50], F. Lefèvre[73], M. Lenhardt[73], L. Leistam[40], J. Lehnert[37], V. Lenti[6], H. León[66], I. León Monzón[31], H. León Vargas[37], P. Lévai[18], X. Li[7], Y. Li[7], R. Lietava[12], S. Lindal[78], V. Lindenstruth[43 ii], C. Lippmann[40], M.A. Lisa[27], O. Listratenko[51], L. Liu[8], V. Loginov[69], S. Lohn[40], X. Lopez[26], M. López Noriega[77], R. López-Ramírez[84], E. López Torres[42], G. Løvhøiden[78], A. Lozea Feijo Soares[93], S. Lu[7], M. Lunardon[79], G. Luparello[101], L. Luquin[73], J.-R. Lutz[99], M. Luvisetto[14], K. Ma[111], R. Ma[74], D.M. Madagodahettige-Don[46], A. Maevskaya[67], M. Mager[33 x], A. Mahajan[48], D.P. Mahapatra[11], A. Maire[99], I. Makhlyueva[40], D. Mal'Kevich[68], M. Malaev[39], K.J. Malagalage[30], I. Maldonado Cervantes[65], M. Malek[77], T. Malkiewicz[49], P. Malzacher[32], A. Mamonov[94], L. Manceau[26], L. Mangotra[48], V. Manko[70], F. Manso[26], V. Manzari[6], Y. Mao[111 xxiv], J. Mareš[82], G.V. Margagliotti[103], A. Margotti[14], A. Marín[32], I. Martashvili[53], P. Martinengo[40], M.I. Martínez[84], A. Martínez Davalos[66], G. Martínez García[73], Y. Maruyama[45], A. Marzari Chiesa[101], S. Masciocchi[32], M. Masera[101], M. Masetti[13], A. Masoni[20], L. Massacrier[62], M. Mastromarco[5], A. Mastroserio[5 x], Z.L. Matthews[12], A. Matyja[29], D. Mayani[65], G. Mazza[102], M.A. Mazzoni[88], F. Meddi[87], A. Menchaca-Rocha[66], P. Mendez Lorenzo[40], M. Meoni[40], J. Mercado Pérez[44], P. Mereu[102], Y. Miake[105], A. Michalon[99], N. Miftakhov[39], J. Milosevic[78], F. Minafra[5], A. Mischke[106], D. Miśkowiec[32], C. Mitu[16], K. Mizoguchi[45], J. Mlynarz[34], B. Mohanty[55], L. Molnar[18 x], M.M. Mondal[55], L. Mon-

taño Zetina[64 xxv], M. Monteno[102], E. Montes[63], M. Morando[79], S. Moretto[79], A. Morsch[40], T. Moukhanova[70], V. Muccifora[38], E. Mudnic[97], S. Muhuri[55], H. Müller[40], M.G. Munhoz[93], J. Munoz[84], L. Musa[40], A. Musso[102], B.K. Nandi[71], R. Nania[14], E. Nappi[6], F. Navach[5], S. Navin[12], T.K. Nayak[55], S. Nazarenko[94], G. Nazarov[94], A. Nedosekin[68], F. Nendaz[62], J. Newby[60], A. Nianine[70], M. Nicassio[6 x], B.S. Nielsen[28], S. Nikolaev[70], V. Nikolic[113], S. Nikulin[70], V. Nikulin[39], B.S. Nilsen[27 xxvi], M.S. Nilsson[78], F. Noferini[14], P. Nomokonov[35], G. Nooren[106], N. Novitzky[49], A. Nyatha[71], C. Nygaard[28], A. Nyiri[78], J. Nystrand[8], A. Ochirov[98], G. Odyniec[10], H. Oeschler[33], M. Oinonen[49] K. Okada[100], Y. Okada[45], M. Oldenburg[40], J. Oleniacz[108], C. Oppedisano[102], F. Orsini[89], A. Ortiz Velasquez[65], G. Ortona[101], C.J. Oskamp[106], A. Oskarsson[61], F. Osmic[40], L. Österman[61], P. Ostrowski[108], I. Otterlund[61], J. Otwinowski[32], G. Øvrebekk[8], K. Oyama[44], K. Ozawa[100], Y. Pachmayer[44], M. Pachr[81], F. Padilla[101], P. Pagano[90], G. Paić[65], F. Painke[43], C. Pajares[92], S. Pal[54 xxvii], S.K. Pal[55], A. Palaha[12], A. Palmeri[24], R. Panse[43], G.S. Pappalardo[24], W.J. Park[32], B. Pastirčák[58], C. Pastore[6], V. Paticchio[6], A. Pavlinov[34], T. Pawlak[108], T. Peitzmann[106], A. Pepato[80], H. Pereira[89], D. Peressounko[70], C. Pérez[64 xviii], D. Perini[40], D. Perrino[5 x], W. Peryt[108], J. Peschek[43 ii], A. Pesci[14], V. Peskov[65 x], Y. Pestov[75], A.J. Peters[40], V. Petráček[81], A. Petridis[4 xix], M. Petris[17], P. Petrov[12], M. Petrovici[17], C. Petta[23], J. Peyré[77], S. Piano[104], A. Piccotti[102], M. Pikna[15], P. Pillot[73], L. Pinsky[46], N. Pitz[37], F. Piuz[40], R. Platt[12], M. Płoskoń[10], J. Pluta[108], T. Pocheptsov[35 xxviii], S. Pochybova[18], P.L.M. Podesta Lerma[31], F. Poggio[101], M.G. Poghosyan[101], K. Polák[82], B. Polichtchouk[83], P. Polozov[68], V. Polyakov[39], B. Pommeresch[8], A. Pop[17], F. Posa[5], V. Pospíšil[81], B. Potukuchi[48], J. Pouthas[77], S.K. Prasad[55], R. Preghenella[13 xxii], F. Prino[102], C.A. Pruneau[34], I. Pshenichnov[67], G. Puddu[19], P. Pujahari[71], A. Pulvirenti[23], A. Punin[94], V. Punin[94], M. Putiš[57], J. Putschke[74], E. Quercigh[40], A. Rachevski[104], A. Rademakers[40], S. Radomski[44], T.S. Räihä[49], J. Rak[49], A. Rakotozafindrabe[89], L. Ramello[1], A. Ramírez Reyes[64], M. Rammler[72], R. Raniwala[47], S. Raniwala[47], S.S. Räsänen[49], I. Rashevskaya[104], S. Rath[11], K.F. Read[53], J. Real[41], K. Redlich[107], R. Renfordt[37], A.R. Reolon[38], A. Reshetin[67], F. Rettig[43 ii], J.-P. Revol[40], K. Reygers[72 xxix], H. Ricaud[99 xxx], L. Riccati[102], R.A. Ricci[59], M. Richter[8], P. Riedler[40], W. Riegler[40], F. Riggi[23], A. Rivetti[102], M. Rodriguez Cahuantzi[84], K. Røed[9], D. Röhrich[40 xxxi], S. Román López[84], R. Romita[5 iv], F. Ronchetti[38], P. Rosinský[40], P. Rosnet[26], S. Rossegger[40], A. Rossi[103], F. Roukoutakis[40 xxxii], S. Rousseau[77], C. Roy[73 xii], P. Roy[54], A.J. Rubio-Montero[63], R. Rui[103], I. Rusanov[44], G. Russo[90], E. Ryabinkin[70], A. Rybicki[29], S. Sadovsky[83], K. Šafařík[40], R. Sahoo[79], J. Saini[55], P. Saiz[40], D. Sakata[105], C.A. Salgado[92], R. Salgueiro Domingues da Silva[40], S. Salur[10], T. Samanta[55], S. Sambyal[48], V. Samsonov[39], L. Šándor[58], A. Sandoval[66], M. Sano[105], S. Sano[100], R. Santo[72], R. Santoro[5], J. Sarkamo[49], P. Saturnini[26], E. Scapparone[14], F. Scarlassara[79], R.P. Scharenberg[109], C. Schiaua[17], R. Schicker[44], H. Schindler[40], C. Schmidt[32], H.R. Schmidt[32], K. Schossmaier[40], S. Schreiner[40], S. Schuchmann[37], J. Schukraft[40], Y. Schutz[73], K. Schwarz[32], K. Schweda[44], G. Scioli[13], E. Scomparin[102], G. Segato[79], D. Semenov[98], S. Senyukov[1], J. Seo[50], S. Serci[19], L. Serkin[65], E. Serradilla[63], A. Sevcenco[16], I. Sgura[5], G. Shabratova[35], R. Shahoyan[40], G. Sharkov[68], N. Sharma[25], S. Sharma[48], K. Shigaki[45], M. Shimomura[105], K. Shtejer[42], Y. Sibiriak[70], M. Siciliano[101], E. Sicking[40 xxxiii], E. Siddi[20], T. Siemiarczuk[107], A. Silenzi[13], D. Silvermyr[76], E. Simili[106], G. Simonetti[5 x], R. Singaraju[55], R. Singh[48], V. Singhal[55], B.C. Sinha[55], T. Sinha[54], B. Sitar[15], M. Sitta[1], T.B. Skaali[78], K. Skjerdal[8], R. Smakal[81], N. Smirnov[74], R. Snellings[3], H. Snow[12], C. Søgaard[28], O. Sokolov[65], A. Soloviev[83], H.K. Soltveit[44], R. Soltz[60], W. Sommer[37], C.W. Son[85], H.S. Son[95], M. Song[96], C. Soos[40], F. Soramel[79], D. Soyk[32], M. Spyropoulou-Stassinaki[4], B.K. Srivastava[109], J. Stachel[44], F. Staley[89], E. Stan[16], G. Stefanek[107], G. Stefanini[40], T. Steinbeck[43 ii], E. Stenlund[61], G. Steyn[22], D. Stocco[101 xxxiv], R. Stock[37], P. Stolpovsky[83], P. Strmen[15], A.A.P. Suaide[93],

M.A. Subieta Vásquez[101], T. Sugitate[45], C. Suire[77], M. Šumbera[86], T. Susa[113], D. Swoboda[40], J. Symons[10], A. Szanto de Toledo[93], I. Szarka[15], A. Szostak[20], M. Szuba[108], M. Tadel[40], C. Tagridis[4], A. Takahara[100], J. Takahashi[21], R. Tanabe[105], D.J. Tapia Takaki[77], H. Taureg[40], A. Tauro[40], M. Tavlet[40], G. Tejeda Muñoz[84], A. Telesca[40], C. Terrevoli[5], J. Thäder[43 ii], R. Tieulent[62], D. Tlusty[81], A. Toia[40], T. Tolyhy[18], C. Torcato de Matos[40], H. Torii[45], G. Torralba[43], L. Toscano[102], F. Tosello[102], A. Tournaire[73 xxxv], T. Traczyk[108], P. Tribedy[55], G. Tröger[43], D. Truesdale[27], W.H. Trzaska[49], G. Tsiledakis[44], E. Tsilis[4], T. Tsuji[100], A. Tumkin[94], R. Turrisi[80], A. Turvey[30], T.S. Tveter[78], H. Tydesjö[40], K. Tywoniuk[78], J. Ulery[37], K. Ullaland[8], A. Uras[19], J. Urbán[57], G.M. Urciuoli[88], G.L. Usai[19], A. Vacchi[104], M. Vala[35 ix], L. Valencia Palomo[66], S. Vallero[44], A. van den Brink[106], N. van der Kolk[3], P. Vande Vyvre[40], M. van Leeuwen[106], L. Vannucci[59], A. Vargas[84], R. Varma[71], A. Vasiliev[70], I. Vassiliev[43 xxxii], M. Vassiliou[4], V. Vechernin[98], M. Venaruzzo[103], E. Vercellin[101], S. Vergara[84], R. Vernet[23 xxxvi], M. Verweij[106], I. Vetlitskiy[68], L. Vickovic[97], G. Viesti[79], O. Vikhlyantsev[94], Z. Vilakazi[22], O. Villalobos Baillie[12], A. Vinogradov[70], L. Vinogradov[98], Y. Vinogradov[94], T. Virgili[90], Y.P. Viyogi[11 xxxvii], A. Vodopianov[35], K. Voloshin[68], S. Voloshin[34], G. Volpe[5], B. von Haller[40], D. Vranic[32], J. Vrláková[57], B. Vulpescu[26], B. Wagner[8], V. Wagner[81], L. Wallet[40], R. Wan[111 xii], D. Wang[111], Y. Wang[44], Y. Wang[111], K. Watanabe[105], Q. Wen[7], J. Wessels[72], J. Wiechula[44], J. Wikne[78], A. Wilk[72], G. Wilk[107], M.C.S. Williams[14], N. Willis[77], B. Windelband[44], C. Xu[111], C. Yang[111], H. Yang[44], A. Yasnopolsky[70], F. Yermia[73], J. Yi[85], Z. Yin[111], H. Yokoyama[105], I-K. Yoo[85], X. Yuan[111 xxxviii], V. Yurevich[35], I. Yushmanov[70], E. Zabrodin[78], B. Zagreev[68], A. Zalite[39], C. Zampolli[40 xxxix], Yu. Zanevsky[35], S. Zaporozhets[35], A. Zarochentsev[98], P. Závada[82], H. Zbroszczyk[108], P. Zelnicek[43], A. Zenin[83], A. Zepeda[64], I. Zgura[16], M. Zhalov[39], X. Zhang[111 i], D. Zhou[111], S. Zhou[7], J. Zhu[111], A. Zichichi[13 xxii], A. Zinchenko[35], G. Zinovjev[52], Y. Zoccarato[62], V. Zycháček[81], and M. Zynovyev[52]

Affiliation notes

[i]Also at[26]
[ii]Also at[36]
[iii]Now at[80]
[iv]Now at[32]
[v]Now at[37]
[vi]Now at[22]
[vii]Now at[17]
[viii]Also at[46]
[ix]Now at[57]
[x]Now at[40]
[xi]Now at[49]
[xii]Now at[99]
[xiii]Now at[6]
[xiv]Now at[72]
[xv]Now at: University of Technology and Austrian Academy of Sciences, Vienna, Austria
[xvi]Also at[60]
[xvii]Also at[40]
[xviii]Now at [115]
[xix]Deceased
[xx]Now at[74]
[xxi]Now at[105]

[xxii] Also at [114]
[xxiii] Now at [5]
[xxiv] Also at [41]
[xxv] Now at [101]
[xxvi] Now at [30]
[xxvii] Now at [89]
[xxviii] Also at [78]
[xxix] Now at [44]
[xxx] Now at [33]
[xxxi] Now at [8]
[xxxii] Now at [4]
[xxxiii] Also at [72]
[xxxiv] Now at [73]
[xxxv] Now at [62]
[xxxvi] Now at: Centre de Calcul IN2P3, Lyon, France
[xxxvii] Now at [55]
[xxxviii] Also at [79]
[xxxix] Also at [14]
[xl] Also at Dipartimento di Fisica dell´Università, Udine, Italy

Collaboration institutes

[1] Dipartimento di Scienze e Tecnologie Avanzate dell'Università del Piemonte Orientale and Gruppo Collegato INFN, Alessandria, Italy
[2] Department of Physics Aligarh Muslim University, Aligarh, India
[3] National Institute for Nuclear and High Energy Physics (NIKHEF), Amsterdam, Netherlands
[4] Physics Department, University of Athens, Athens, Greece
[5] Dipartimento Interateneo di Fisica 'M. Merlin' and Sezione INFN, Bari, Italy
[6] Sezione INFN, Bari, Italy
[7] China Institute of Atomic Energy, Beijing, China
[8] Department of Physics and Technology, University of Bergen, Bergen, Norway
[9] Faculty of Engineering, Bergen University College, Bergen, Norway
[10] Lawrence Berkeley National Laboratory, Berkeley, California, United States
[11] Institute of Physics, Bhubaneswar, India
[12] School of Physics and Astronomy, University of Birmingham, Birmingham, United Kingdom
[13] Dipartimento di Fisica dell'Università and Sezione INFN, Bologna, Italy
[14] Sezione INFN, Bologna, Italy
[15] Faculty of Mathematics, Physics and Informatics, Comenius University, Bratislava, Slovakia
[16] Institute of Space Sciences (ISS), Bucharest, Romania
[17] National Institute for Physics and Nuclear Engineering, Bucharest, Romania
[18] KFKI Research Institute for Particle and Nuclear Physics, Hungarian Academy of Sciences, Budapest, Hungary
[19] Dipartimento di Fisica dell'Università and Sezione INFN, Cagliari, Italy
[20] Sezione INFN, Cagliari, Italy
[21] Universidade Estadual de Campinas (UNICAMP), Campinas, Brazil
[22] Physics Department, University of Cape Town, iThemba Laboratories, Cape Town, South Africa
[23] Dipartimento di Fisica e Astronomia dell'Università and Sezione INFN, Catania, Italy

[24] Sezione INFN, Catania, Italy
[25] Physics Department, Panjab University, Chandigarh, India
[26] Laboratoire de Physique Corpusculaire (LPC), Clermont Université, Université Blaise Pascal, CNRS–IN2P3, Clermont-Ferrand, France
[27] Department of Physics, Ohio State University, Columbus, Ohio, United States
[28] Niels Bohr Institute, University of Copenhagen, Copenhagen, Denmark
[29] The Henryk Niewodniczanski Institute of Nuclear Physics, Polish Academy of Sciences, Cracow, Poland
[30] Physics Department, Creighton University, Omaha, Nebraska, United States
[31] Universidad Autónoma de Sinaloa, Culiacán, Mexico
[32] ExtreMe Matter Institute EMMI, GSI Helmholtzzentrum für Schwerionenforschung, Darmstadt, Germany
[33] Institut für Kernphysik, Technische Universität Darmstadt, Darmstadt, Germany
[34] Wayne State University, Detroit, Michigan, United States
[35] Joint Institute for Nuclear Research (JINR), Dubna, Russia
[36] Frankfurt Institute for Advanced Studies, Johann Wolfgang Goethe-Universität Frankfurt, Frankfurt, Germany
[37] Institut für Kernphysik, Johann Wolfgang Goethe-Universität Frankfurt, Frankfurt, Germany
[38] Laboratori Nazionali di Frascati, INFN, Frascati, Italy
[39] Petersburg Nuclear Physics Institute, Gatchina, Russia
[40] European Organization for Nuclear Research (CERN), Geneva, Switzerland
[41] Laboratoire de Physique Subatomique et de Cosmologie (LPSC), Université Joseph Fourier, CNRS-IN2P3, Institut Polytechnique de Grenoble, Grenoble, France
[42] Centro de Aplicaciones Tecnológicas y Desarrollo Nuclear (CEADEN), Havana, Cuba
[43] Kirchhoff-Institut für Physik, Ruprecht-Karls-Universität Heidelberg, Heidelberg, Germany
[44] Physikalisches Institut, Ruprecht-Karls-Universität Heidelberg, Heidelberg, Germany
[45] Hiroshima University, Hiroshima, Japan
[46] University of Houston, Houston, Texas, United States
[47] Physics Department, University of Rajasthan, Jaipur, India
[48] Physics Department, University of Jammu, Jammu, India
[49] Helsinki Institute of Physics (HIP) and University of Jyväskylä, Jyväskylä, Finland
[50] Kangnung National University, Kangnung, South Korea
[51] Scientific Research Technological Institute of Instrument Engineering, Kharkov, Ukraine
[52] Bogolyubov Institute for Theoretical Physics, Kiev, Ukraine
[53] University of Tennessee, Knoxville, Tennessee, United States
[54] Saha Institute of Nuclear Physics, Kolkata, India
[55] Variable Energy Cyclotron Centre, Kolkata, India
[56] Fachhochschule Köln, Köln, Germany
[57] Faculty of Science, P.J. Šafárik University, Košice, Slovakia
[58] Institute of Experimental Physics, Slovak Academy of Sciences, Košice, Slovakia
[59] Laboratori Nazionali di Legnaro, INFN, Legnaro, Italy
[60] Lawrence Livermore National Laboratory, Livermore, California, United States
[61] Division of Experimental High Energy Physics, University of Lund, Lund, Sweden
[62] Université de Lyon 1, CNRS/IN2P3, Institut de Physique Nucléaire de Lyon, Lyon, France
[63] Centro de Investigaciones Energéticas Medioambientales y Tecnológicas (CIEMAT), Madrid, Spain
[64] Centro de Investigación y de Estudios Avanzados (CINVESTAV), Mexico City and Mérida, Mexico

[65] Instituto de Ciencias Nucleares, Universidad Nacional Autónoma de México, Mexico City, Mexico
[66] Instituto de Física, Universidad Nacional Autónoma de México, Mexico City, Mexico
[67] Institute for Nuclear Research, Academy of Sciences, Moscow, Russia
[68] Institute for Theoretical and Experimental Physics, Moscow, Russia
[69] Moscow Engineering Physics Institute, Moscow, Russia
[70] Russian Research Centre Kurchatov Institute, Moscow, Russia
[71] Indian Institute of Technology, Mumbai, India
[72] Institut für Kernphysik, Westfälische Wilhelms-Universität Münster, Münster, Germany
[73] SUBATECH, Ecole des Mines de Nantes, Université de Nantes, CNRS-IN2P3, Nantes, France
[74] Yale University, New Haven, Connecticut, United States
[75] Budker Institute for Nuclear Physics, Novosibirsk, Russia
[76] Oak Ridge National Laboratory, Oak Ridge, Tennessee, United States
[77] Institut de Physique Nucléaire d'Orsay (IPNO), Université Paris-Sud, CNRS-IN2P3, Orsay, France
[78] Department of Physics, University of Oslo, Oslo, Norway
[79] Dipartimento di Fisica dell'Università and Sezione INFN, Padova, Italy
[80] Sezione INFN, Padova, Italy
[81] Faculty of Nuclear Sciences and Physical Engineering, Czech Technical University in Prague, Prague, Czech Republic
[82] Institute of Physics, Academy of Sciences of the Czech Republic, Prague, Czech Republic
[83] Institute for High Energy Physics, Protvino, Russia
[84] Benemérita Universidad Autónoma de Puebla, Puebla, Mexico
[85] Pusan National University, Pusan, South Korea
[86] Nuclear Physics Institute, Academy of Sciences of the Czech Republic, Řež u Prahy, Czech Republic
[87] Dipartimento di Fisica dell'Università 'La Sapienza' and Sezione INFN, Rome, Italy
[88] Sezione INFN, Rome, Italy
[89] Commissariat à l'Energie Atomique, IRFU, Saclay, France
[90] Dipartimento di Fisica 'E.R. Caianiello' dell'Università and Sezione INFN, Salerno, Italy
[91] California Polytechnic State University, San Luis Obispo, California, United States
[92] Departamento de Física de Partículas and IGFAE, Universidad de Santiago de Compostela, Santiago de Compostela, Spain
[93] Universidade de São Paulo (USP), São Paulo, Brazil
[94] Russian Federal Nuclear Center (VNIIEF), Sarov, Russia
[95] Department of Physics, Sejong University, Seoul, South Korea
[96] Yonsei University, Seoul, South Korea
[97] Technical University of Split FESB, Split, Croatia
[98] V. Fock Institute for Physics, St. Petersburg State University, St. Petersburg, Russia
[99] Institut Pluridisciplinaire Hubert Curien (IPHC), Université de Strasbourg, CNRS-IN2P3, Strasbourg, France
[100] University of Tokyo, Tokyo, Japan
[101] Dipartimento di Fisica Sperimentale dell'Università and Sezione INFN, Turin, Italy
[102] Sezione INFN, Turin, Italy
[103] Dipartimento di Fisica dell'Università and Sezione INFN, Trieste, Italy
[104] Sezione INFN, Trieste, Italy
[105] University of Tsukuba, Tsukuba, Japan

[106] Institute for Subatomic Physics, Utrecht University, Utrecht, Netherlands
[107] Soltan Institute for Nuclear Studies, Warsaw, Poland
[108] Warsaw University of Technology, Warsaw, Poland
[109] Purdue University, West Lafayette, Indiana, United States
[110] Zentrum für Technologietransfer und Telekommunikation (ZTT), Fachhochschule Worms, Worms, Germany
[111] Hua-Zhong Normal University, Wuhan, China
[112] Yerevan Physics Institute, Yerevan, Armenia
[113] Rudjer Bošković Institute, Zagreb, Croatia
[114] Centro Fermi – Centro Studi e Ricerche e Museo Storico della Fisica "Enrico Fermi", Rome, Italy
[115] Sección Física, Departamento de Ciencias, Pontificia Universidad Católica del Perú, Lima, Peru

Corresponding author: Andrea Dainese (andrea.dainese@pd.infn.it)

1. Introduction

The ALICE experiment [1] will study nucleus–nucleus, proton–proton and proton–nucleus collisions at the CERN Large Hadron Collider (LHC). The main physics goal of the experiment is to investigate the properties of strongly-interacting matter in the conditions of high energy density (> 10 GeV/fm^3) and high temperature ($\gtrsim 0.2$ GeV), expected to be reached in central Pb–Pb collisions at $\sqrt{s_{\rm NN}} = 5.5$ TeV. Under these conditions, according to lattice QCD calculations, quark confinement into colourless hadrons should be removed and a deconfined Quark–Gluon Plasma should be formed [2]. In the past two decades, experiments at CERN-SPS ($\sqrt{s_{\rm NN}} = 17.3$ GeV) and BNL-RHIC ($\sqrt{s_{\rm NN}} = 200$ GeV) have gathered ample evidence for the formation of this state of matter [3].

The ALICE experimental apparatus, shown in Fig. 1, consists of a central barrel, a forward muon spectrometer and a set of small detectors in the forward regions for trigger and other functions. The coverage of the central barrel detectors allows the tracking of particles emitted within a pseudo-rapidity range $|\eta| < 0.9$ over the full azimuth. The central barrel is surrounded by the large L3 magnet that provides a field B $= 0.5$ T.

The ITS (Inner Tracking System) is a cylindrically-shaped silicon tracker that surrounds the interaction region. It consists of six layers, with radii between 3.9 cm and 43.0 cm, covering the pseudo-rapidity range $|\eta| < 0.9$. The two innermost layers are equipped with Silicon Pixel Detectors (SPD), the two intermediate layers contain Silicon Drift Detectors (SDD), while Silicon Strip Detectors (SSD) are used on the two outermost layers. The main task of the ITS is to provide precise track and vertex reconstruction close to the interaction point. In particular, the ITS was designed with the aim to improve the position, angle, and momentum resolution for tracks

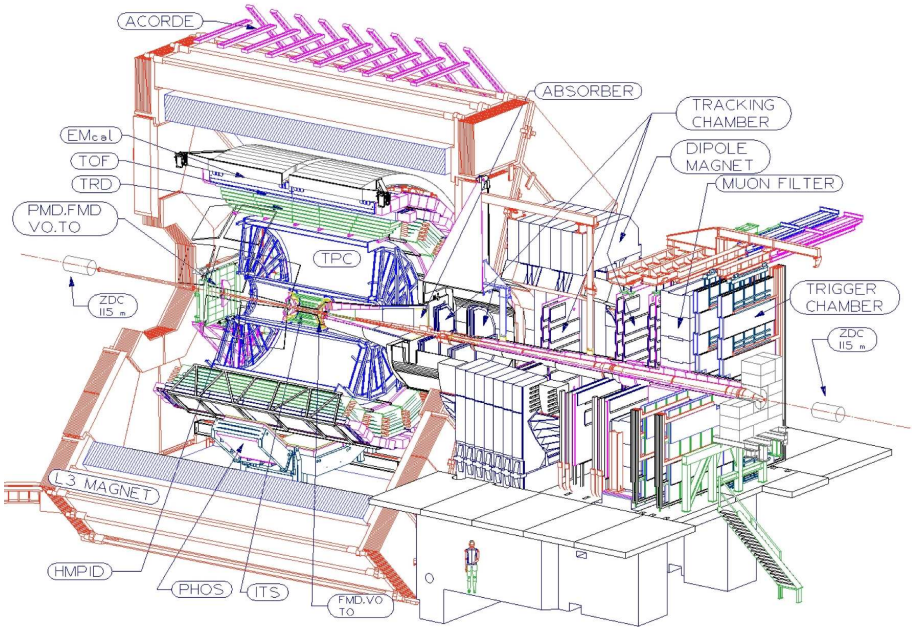

Figure 1. General layout of the ALICE experiment [1].

reconstructed in the Time Projection Chamber (TPC), to identify the secondary vertices from the decay of hyperons and heavy flavoured hadrons, to reconstruct the interaction vertex with a resolution better than 100 μm, and to recover particles that are missed by the TPC due to acceptance limitations (very low momentum particles not reaching the TPC and very high momentum ones propagating along the 10% inactive area between adjacent TPC chambers).

The measurement of charm and beauty hadron production in Pb–Pb collisions at the LHC is one of the main items of the ALICE physics program, because it will allow to investigate the mechanisms of heavy-quark propagation and hadronization in the large, hot and dense medium formed in high-energy heavy-ion collisions and it will serve as a reference for the study of the effects of the medium on quarkonia states [4]. To measure the separation, from the interaction vertex, of the decay vertices of heavy flavoured hadrons, which have mean proper decay lengths $c\tau \sim 100$–500 μm, requires a resolution on the track impact parameter (distance of closest approach to the vertex) well below 100 μm. This requirement is met by the ITS. The design position resolution in the plane transverse to the beam line for charged-pion tracks reconstructed in the TPC and in the ITS is expected to be approximately $10\ \mu\mathrm{m} + 53\ \mu\mathrm{m}/(p_\mathrm{t}\sqrt{\sin\theta})$, where p_t is the transverse momentum in GeV/c and θ is the polar angle with respect to the beam line [4]. The ITS is made of thousands of separate modules, whose position is different from the ideal due to the limitations associated with the assembly and integration of the different components, and the forces these components experience. In order to achieve the required high precision on the track parameters, the relative position (location and orientation) of every module needs to be determined precisely. We refer to the procedure used to determine the modules relative position as alignment. The ITS alignment procedure starts from the positioning survey measurements performed during the assembly, and is refined using tracks from cosmic-ray muons and from particles produced in LHC pp collisions. Two independent methods, based on tracks-to-measured-points residuals minimization, are considered. The first method uses the Millepede approach [5], where a global fit to all residuals is performed, extracting all the alignment parameters simultaneously. The second method performs a (local) minimization for each single module and accounts for correlations between modules by iterating the procedure until convergence is reached.

In this article, we present the alignment methods for the ITS and the results obtained using the cosmic-data sample collected during summer 2008 with B = 0 (a small data set with B = $\pm$0.5 T was also collected; we used it for a few specific validation checks). In section 2 we describe in detail the ITS detector layout and in section 3 we discuss the strategy adopted for the alignment. In section 4 we describe the 2008 sample of cosmic-muon data. These data were used to validate the available survey measurements (section 5) and to apply the track-based alignment algorithms: the Millepede method (section 6) and a local method that we are developing (section 7). We draw conclusions in section 8.

2. ITS detector layout

The geometrical layout of the ITS layers is shown in the left-hand panel of Fig. 2, as it is implemented in the ALICE simulation and reconstruction software framework (AliRoot [6]). The ALICE global reference system has the z axis on the beam line, the x axis in the LHC (horizontal) plane, pointing to the centre of the accelerator, and the y axis pointing upward. The axis of the ITS

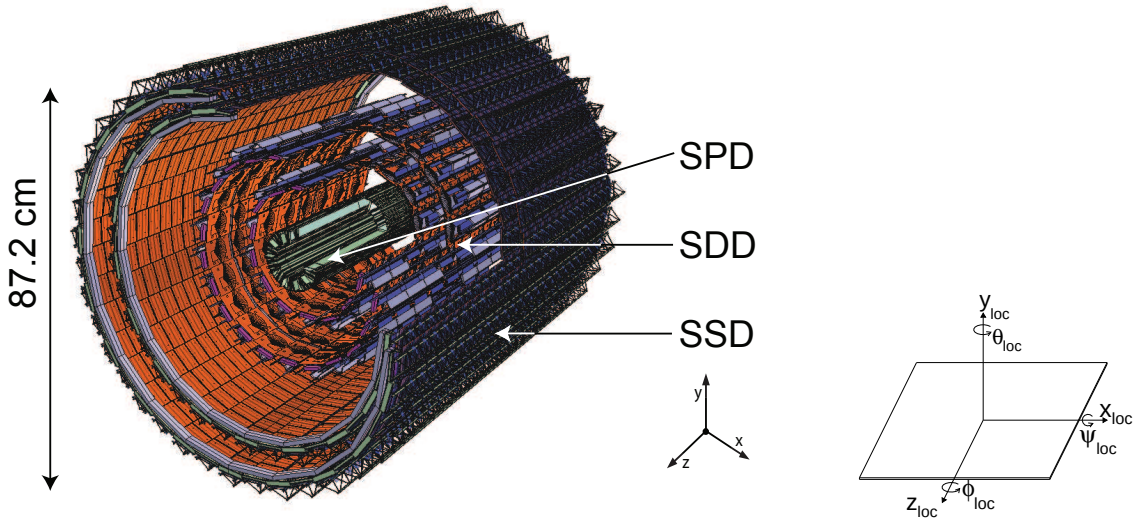

Figure 2. Layout of the ITS (left) and orientation of the ALICE global (middle) and ITS-module local (right) reference systems. The global reference system has indeed its origin in the middle of the ITS, so that the z direction coincides with the beam line.

barrel coincides with the z axis. The module local reference system (Fig. 2, right) is defined with the $x_{\rm loc}$ and $z_{\rm loc}$ axes on the sensor plane and with the $z_{\rm loc}$ axis in the same direction as the global z axis. The local x direction is approximately equivalent to the global $r\varphi$. The alignment degrees of freedom of the module are translations in $x_{\rm loc}$, $y_{\rm loc}$, $z_{\rm loc}$, and rotations by angles $\psi_{\rm loc}$, $\theta_{\rm loc}$, $\varphi_{\rm loc}$, about the $x_{\rm loc}$, $y_{\rm loc}$, $z_{\rm loc}$ axes, respectively[1].

The ITS geometry in AliRoot is described in full detail, down to the level of all mechanical structures and single electronic components, using the ROOT [7] geometrical modeler. This detailed geometry is used in Monte Carlo simulations and in the track reconstruction procedures, thereby accounting for the exact position of the sensor modules and of all the passive material that determine particle scattering and energy loss.

The geometrical parameters of the layers (radial position, length along beam axis, number of modules, spatial resolution, and material budget) are summarized in Table 1. The material budget reported in the table takes into account the ϕ-averaged material (including the sensors, electronics, cabling, support structures, and cooling) associated with radial paths through each layer. Another 1.30% of radiation length comes from the thermal shields and supports installed between SPD and SDD barrels and between SDD and SSD barrels, thus making the total material budget for perpendicular tracks equal to 7.66% of X_0.

In the following, the features of each of the three sub-detectors (SPD, SDD and SSD) that are relevant for alignment issues are described (for more details see [1]).

2.1 Silicon Pixel Detector (SPD)

The basic building block of the ALICE SPD is a module consisting of a two-dimensional sensor matrix of reverse-biased silicon detector diodes bump-bonded to 5 front-end chips. The sensor

[1]The alignment transformation can be expressed equivalently in terms of the local or global coordinates.

Table 1. Characteristics of the six ITS layers.

Layer	Type	r [cm]	$\pm z$ [cm]	Number of modules	Active Area per module $r\varphi \times z$ [mm^2]	Resolution $r\varphi \times z$ [μm^2]	Material budget X/X_0 [%]
1	pixel	3.9	14.1	80	12.8×70.7	12×100	1.14
2	pixel	7.6	14.1	160	12.8×70.7	12×100	1.14
3	drift	15.0	22.2	84	70.17×75.26	35×25	1.13
4	drift	23.9	29.7	176	70.17×75.26	35×25	1.26
5	strip	38.0	43.1	748	73×40	20×830	0.83
6	strip	43.0	48.9	950	73×40	20×830	0.86

matrix consists of 256 × 160 cells, each measuring 50 μm ($r\varphi$) by 425 μm (z).

Two modules are mounted together along the z direction to form a 141.6 mm long half-stave. Two mirrored half-staves are attached, head-to-head along the z direction, to a carbon-fibre support sector, which also provides cooling. Each sector (see Fig. 3, right) supports six staves: two on the inner layer and four on the outer layer. The sensors are mounted in such a way that there is a 2% overlap between the active regions in $r\varphi$, but along z there is a gap between each two consecutive sensors. Five sectors are then mounted together to form a half-barrel and finally the two (top and bottom) half-barrels are mounted around the beam pipe to close the full barrel (shown in the left-hand side of Fig. 3), which is actually composed of 10 sectors. In total, the SPD includes 60 staves, consisting of 240 modules with 1200 readout chips for a total of 9.8×10^6 cells.

The spatial precision of the SPD sensor is determined by the pixel cell size, the track incidence angle on the detector, and by the threshold applied in the readout electronics. The values of resolution along $r\varphi$ and z extracted from beam tests are 12 and 100 μm, respectively.

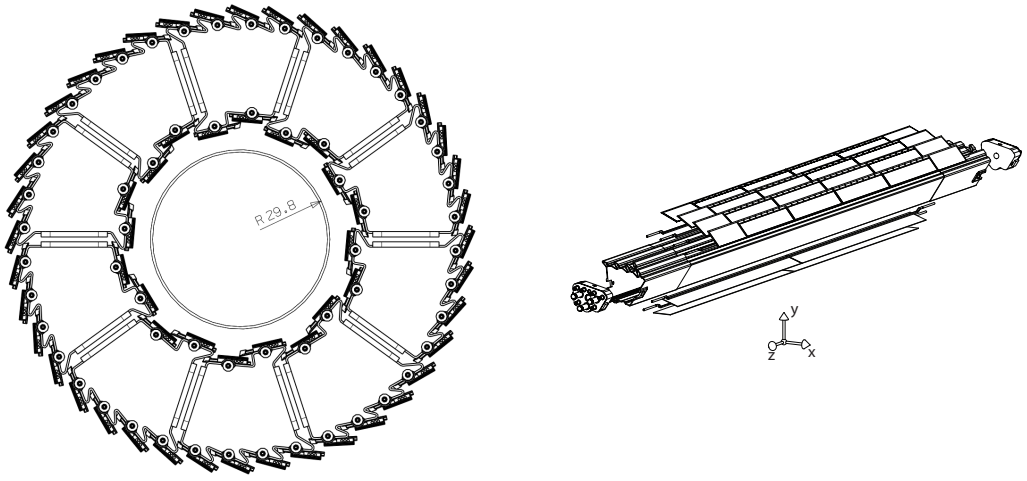

Figure 3. SPD drawings. Left: the SPD barrel and the beam pipe (radius in mm). Right: a Carbon Fibre Support Sector.

2.2 Silicon Drift Detector (SDD)

The basic building block of the ALICE SDD [8] is a module divided into two drift regions where electrons move in opposite directions under a drift field of ≈ 500 V/cm (see Fig. 4, right), with hybrids housing the front-end electronics on either side. The SDD modules are mounted on linear structures called ladders. There are 14 ladders with six modules each on the inner SDD layer (layer 3), and 22 ladders with eight modules each on the outer SDD layer (layer 4). Modules and ladders are assembled to have an overlap of the sensitive areas larger than 580 μm in both $r\varphi$ and z directions, so as to provide full angular coverage over the pseudo-rapidity range $|\eta| < 0.9$ (Fig. 4, left).

The modules are attached to the ladder space frame and have their anode rows parallel to the ladder axis (z). The ladders are mounted on a support structure made of two cones and four support rings to form the two cylindrical layers [9]. The support rings are mechanically fixed to the cones and bear ruby spheres, used as a reference for the ladder positioning as well as for the geometrical survey of the module positions in the ladder reference system.

The z coordinate is reconstructed from the centroid of the collected charge along the anodes. The position along the drift coordinate ($x_{\rm loc} \approx r\varphi$) is reconstructed starting from the measured drift time with respect to the trigger time. An unbiased reconstruction of the $x_{\rm loc}$ coordinate requires therefore to know with good precision the drift velocity and the time-zero (t_0), which is the measured drift time for particles with zero drift distance. The drift velocity depends on temperature (as $T^{-2.4}$) and it is therefore sensitive to temperature gradients in the SDD volume and to temperature variations with time. Hence, it is important to calibrate this parameter frequently during the data taking. Three rows of 33 MOS charge injectors are implanted at known distances from the collection anodes in each of the two drift regions of a SDD module [10] for this purpose, as sketched in Fig. 4 (right). Finally, a correction for non-uniformity of the drift field (due to non-linearities in the voltage divider and, for a few modules, also due to significant inhomogeneities in dopant concentration) has to be applied. This correction is extracted from measurements of the systematic deviations between charge injection position and reconstructed coordinates that was performed on

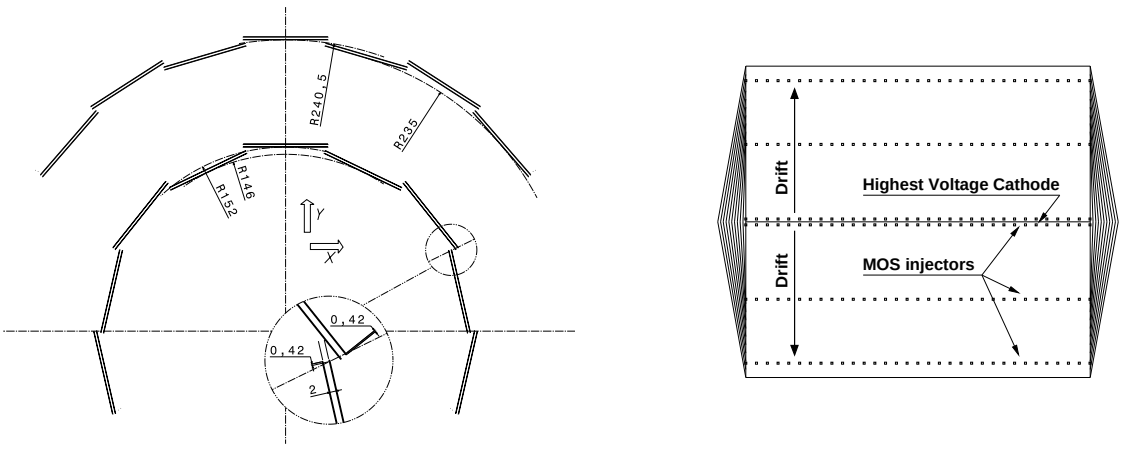

Figure 4. Left: scheme of the SDD layers. Right: scheme of a SDD module, where the drift direction is parallel to the $x_{\rm loc}$ coordinate. Units are millimeters.

all the 260 SDD modules with an infrared laser [11].

The spatial precision of the SDD detectors, as obtained during beam tests of full-size prototypes, is on average 35 μm along the drift direction $x_{\rm loc}$ and 25 μm for the anode coordinate $z_{\rm loc}$.

2.3 Silicon Strip Detector (SSD)

The basic building block of the ALICE SSD is a module composed of one double-sided strip detector connected to two hybrids hosting the front-end electronics. Each sensor has 768 strips on each side with a pitch of 95 μm. The stereo angle is 35 mrad, which is a compromise between stereo view and reduction of ambiguities resulting from high particle densities. The strips are almost parallel to the beam axis (z-direction), to provide the best resolution in the $r\varphi$ direction.

The modules are assembled on ladders of the same design as those supporting the SDD [9]. A view of the SSD ladder is shown in Fig. 5. The innermost SSD layer (layer 5) is composed of 34 ladders, each of them being a linear array of 22 modules along the beam direction. Layer 6 (the outermost ITS layer) consists of 38 ladders, each made of 25 modules. In order to obtain full pseudo-rapidity coverage, the modules are mounted on the ladders with small overlaps between successive modules, that are staggered by 600 μm in the radial direction. The 72 ladders, carrying a total of 1698 modules, are mounted on support cones in two cylinders. Carbon fiber is lightweight (to minimize the interactions) and at the same time it is a stiff material allowing to minimize the bending due to gravity, which is expected to give shifts of at most 50 μm, for the modules at the centre of the lateral ladders of the outer SSD layer.

For each layer, neighbouring ladders are mounted at one of two slightly different radii ($\Delta r =$ 6 mm) such that full azimuthal coverage is obtained. The acceptance overlaps, present both along z and $r\varphi$, amount to 2% of the SSD sensor surface. The positions of the sensors with respect to reference points on the ladder were measured during the detector construction phase, as well as the ones of the ladders with respect to the support cones.

The spatial resolution of the SSD system is determined by the 95 μm pitch of the sensor readout strips and the charge-sharing between those strips. Without making use of the analogue information the r.m.s spatial resolution is 27 μm. Beam tests [12] have shown that a spatial resolution of better than 20 μm in the rφ direction can be obtained by analyzing the charge distribution within each cluster. In the direction along the beam, the spatial resolution is of about 830 μm.

The SSD gain calibration has two components: overall calibration of ADC values to energy loss and relative calibration of the P and N sides. This charge matching is a strong point of double sided silicon sensors and helps to remove fake clusters. Both the overall and relative calibration

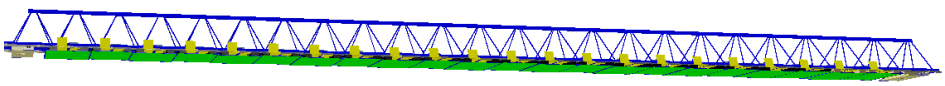

Figure 5. View of one SSD ladder (from layer 5) as described in the AliRoot geometry.

are obtained from the data. Since the signal-to-noise ratio is larger than 20, the detection efficiency does not depend much on the details of the gain calibration.

3. Alignment target and strategy

For silicon tracking detectors, the typical target of the alignment procedures is to achieve a level of precision and accuracy such that the resolution on the reconstructed track parameters (in particular, the impact parameter and the curvature, which measures the transverse momentum) is not degraded significantly with respect to the resolution expected in case of the ideal geometry without misalignment. For the ALICE ITS, this maximum acceptable degradation has been conventionally set to 20% (a similar target is adopted also for the ATLAS Inner Detector [13]). The resolutions on the track impact parameter and curvature are both proportional to the space point resolution, in the limit of negligible multiple scattering effect (large momentum). If the residual misalignment is assumed to be equivalent to random gaussian spreads in the six alignment parameters of the sensor modules, on which space points are measured, a 20% degradation in the effective space point resolution (hence 20% degradation of the track parameters in the large momentum limit) is obtained when the misalignment spread in a given direction is $\sqrt{120\%^2 - 100\%^2} \approx 70\%$ of the intrinsic sensor resolution along that direction. With reference to the intrinsic precisions listed in Table 1, the target residual misalignment spreads in the local coordinates on the sensor plane are: for SPD, 8 μm in $x_{\rm loc}$ and 70 μm in $z_{\rm loc}$; for SDD, 25 μm in $x_{\rm loc}$ and 18 μm in $z_{\rm loc}$; for SSD, 14 μm in $x_{\rm loc}$ and 500 μm in $z_{\rm loc}$. Note that these spreads represent effective alignment spreads, including the significant effect of the $\theta_{\rm loc}$ angle (rotation about the axis normal to the sensor plane) on the spatial resolution. In any case, these target numbers are only an indication of the precision that is required to reach an acceptable alignment quality. We will aim at getting even closer to the design performance expected in case of ideal geometry.

The other alignment parameters ($y_{\rm loc}$, $\psi_{\rm loc}$, $\varphi_{\rm loc}$) describe movements of the modules mainly in the radial direction. These have a small impact on the effective resolution, for tracks with a small angle with respect to the normal to the module plane, a typical case for tracks coming from the interaction region. However, they are related to the so-called *weak modes*: correlated misalignments of the different modules that do not affect the reconstructed tracks fit quality (χ^2), but bias systematically the track parameters. A typical example is radial expansion or compression of all the layers, which biases the measured track curvature, hence the momentum estimate. Correlated misalignments for the parameters on the sensor plane ($x_{\rm loc}$, $z_{\rm loc}$, $\theta_{\rm loc}$) can determine weak modes as well. These misalignments are, by definition, difficult to determine with tracks from collisions, but can be addressed using physical observables [14] (e.g. looking for shift in invariant masses of reconstructed decay particles) and cosmic-ray tracks. These offer a unique possibility to correlate modules that are never correlated when using tracks from the interaction region, and they offer a broad range of track-to-module-plane incidence angles that help to constrain also the $y_{\rm loc}$, $\psi_{\rm loc}$ and $\varphi_{\rm loc}$ parameters, thus improving the sensitivity to weak modes.

As already mentioned in the introduction, the sources of alignment information that we use are the survey measurements and the reconstructed space points from cosmic-ray and collision particles. These points are the input for the software alignment methods, based on global or local minimization of the residuals.

The general strategy for the ITS first alignment starts with the validation of the construction survey measurements of the SSD detector with cosmic-ray tracks and continues with the software alignment of the SPD and the SSD detectors, which also uses cosmic-ray tracks, collected without magnetic field. The initial alignment is more robust if performed with straight tracks (no field), which help to avoid possible biases that can be introduced when working with curved tracks (e.g. radial layer compression/expansion). Then, the already aligned SPD and SSD are used to confirm and refine the initial time-zero calibration of SDD, obtained with SDD standalone methods. These first steps are described in this report, which presents the status of the ITS alignment before the start of the LHC with proton–proton collisions.

The next step will be, after the validation of the SDD survey measurements with cosmic-ray tracks, the alignment of the full detector (SPD, SDD, SSD) with tracks from cosmic rays and, mainly, from proton–proton collisions collected with magnetic field B = 0 and B = 0.5 T. In particular, the data with magnetic field switched on will allow us to study the track quality and precision as a function of the measured track momentum, thus separating the detector resolution and residual misalignment from multiple scattering. The tracks from collisions will provide a uniform coverage of the detector modules and will also be used to routinely monitor the quality of the alignment during data taking, and refine the corrections if needed. The last step will be the relative alignment of the ITS and the TPC with tracks, when both detectors will be internally aligned and calibrated. In addition, the relative movement of the ITS with respect to the TPC is being monitored, and to some extent measured, using a dedicated system based on lasers, mirrors and cameras [15].

4. Cosmic-ray run 2008: data taking and reconstruction

During the 2008 cosmic run, extending from June to October, about 10^5 events with reconstructed tracks in the ITS were collected. In order to simplify the first alignment round, the solenoidal magnetic field was switched off during most of this data taking period. The status of the three ITS sub-detectors during the data taking is summarized in the following paragraph (for more details on the sub-detectors commissioning, see Refs. [16–18]). The corresponding status during the first LHC runs with proton–proton collisions is given in Ref. [19].

For the SPD, 212 out of 240 modules (88%) were active. Noisy pixels, corresponding to less than 0.15% of the total number of pixels, were masked out, and the information was stored in the Offline Conditions Database (OCDB) to be used in the offline reconstruction. For the SDD, 246 out of 260 modules (95%) participated in the data acquisition. The baseline, gain and noise for each of the 133,000 anodes were measured every 24 hours by means of dedicated calibration runs that allowed us also to tag noisy ($\approx 0.5\%$) and dead (1%) channels. The drift velocities were measured with dedicated injector runs collected every 6 hours, stored in the OCDB and successively used in the reconstruction. For the SSD, 1477 out of 1698 modules (87%) were active. The fraction of bad strips was $\approx 1.5\%$. The normalized difference in P- and N-charge had a FWHM of 11%. The gains proved to be stable during the data taking.

The events to be used for the ITS alignment were collected with a trigger provided by the pixel detectors (SPD). The SPD FastOR trigger [1] is based on a programmable hit pattern recognition system (on FPGA) at the level of individual readout chips (1200 in total, each reading a sensor area

of about 1.4×1.4 cm^2). This trigger system allows for a flexible selection of events of interest, for example high-multiplicity proton–proton collisions, foreseen to be studied in the scope of the ALICE physics program. For the 2008 cosmic run, the trigger logic consisted of selecting events with at least one hit on the upper half of the outer SPD layer ($r \approx 7$ cm) and at least one on the lower half of the same layer. This trigger condition enhances significantly the probability of selecting events in which a cosmic muon, coming from above (the dominant component of the cosmic-ray particles reaching the ALICE cavern placed below ≈ 30 m of molasse), traverses the full ITS detector. This FastOR trigger is very efficient (more than 99%) and has purity (fraction of events with a reconstructed track having points in both SPD layers) reaching about 30–40%, limited mainly by the radius of the inner layer (≈ 4 cm) because the trigger assures only the passage of a particle through the outer layer (≈ 7 cm). For the FastOR trigger, typically 77% of the chips (i.e. about 90% of the active modules) could be configured and used. The trigger rate was about 0.18 Hz.

The following procedure, fully integrated in the AliRoot framework [6], is used for track reconstruction. After the cluster finding in the ITS (hereafter, we will refer to the clusters as "points"), a pseudo primary vertex is created using three aligned points in two consecutive layers (starting the search from the SPD). Track reconstruction is then performed using the ITS standalone tracker (as described in [4, 20]), which finds tracks in the outward direction, from the innermost SPD layer to the outermost SSD layer, using the previously found pseudo primary vertex as its seed; all found tracks are then refitted using the standard Kalman-filter fit procedure as implemented in the default ITS tracker. During the track refit stage, when the already identified ITS points are used in the Kalman-filter fit in the inward direction, in order to obtain the track parameters estimate at the (pseudo) vertex, "extra" points are searched for in the ITS module overlaps. For each layer, a search road for these overlap points in the neighbouring modules is defined with a size of about seven times the current track position error. Currently, the "extra" points are not used to update the track parameters, so they can be exploited as a powerful tool to evaluate the ITS alignment quality.

A clean cosmic event consists of two separate tracks, one "incoming" in the top part of the ITS and one "outgoing" in the bottom part. Their matching at the reference median plane ($y = 0$) can be used as another alignment quality check. These two track halves are merged together in a single array of track points, which is the single-event input for the track-based alignment algorithms. A typical event of this type, as visualized in the ALICE event display, is shown in Fig. 6.

The uncorrected zenith-azimuth 2D distribution of the (merged) tracks with at least eight points in the ITS is shown in Fig. 7, where the azimuth angle is defined in a horizontal plane starting from the positive side of the z global axis. The modulations in the azimuthal dependence of the observed flux are due to the presence of inhomogeneities in the molasse above the ALICE cavern, mainly the presence of two access shafts. These are seen as the structures at zenith angle $\approx 30^\circ$ and azimuth $\approx 180^\circ$ (large shaft) and $\approx 270^\circ$ (small shaft). On top of these structures, the effect of the SPD outer layer geometrical acceptance is visible: the azimuthal directions perpendicular to the z axis (around 90° and 270°) have larger acceptance in the zenith angle.

The main limitation of the usage of cosmic-ray tracks for the alignment of a cylindrical detector like the ITS is that the occupancy of the side modules (zenith angles approaching 90°) is small, especially for the external layers [21]. In the case of the SSD outer layer, which has the smallest fractional coverage, about 75% of the ladders are covered. This is due to the small size

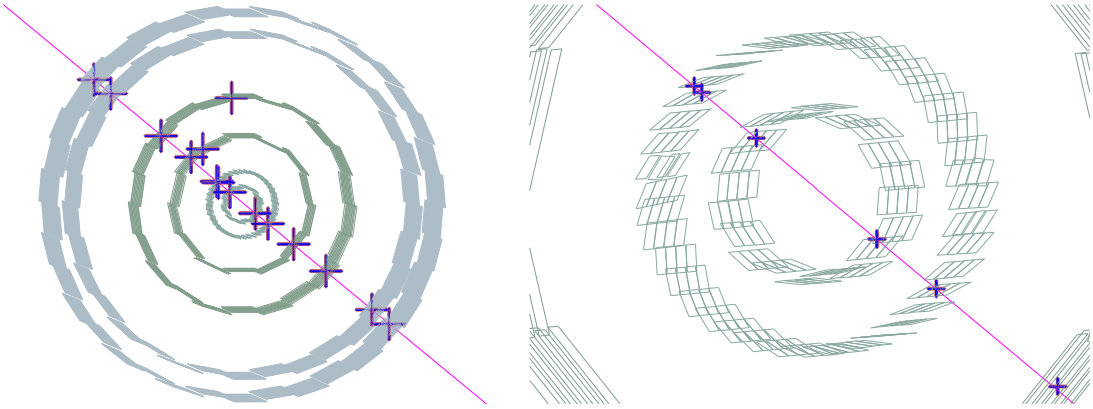

Figure 6. (colour online) A clean cosmic event reconstructed in the ITS (left), as visualized in the ALICE event display. The zoom on the SPD (right) shows an "extra" point in one of the $r\varphi$ acceptance overlaps of the outer layer.

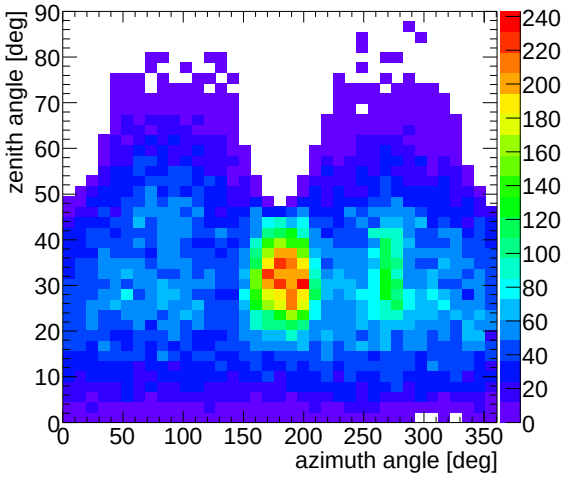

Figure 7. (colour online) Uncorrected distribution of the zenith-azimuth angles of the cosmic tracks reconstructed in the ITS.

of the triggering detector (SPD), the dominance of small zenith angles for cosmic-ray particles and the cut on the track-to-module incidence angle ($> 30^{\circ}$) that we apply to reject large and elongated clusters.

5. Validation of the survey measurements with cosmic-ray tracks

The SDD and SSD were surveyed during the assembling phase using a measuring machine. The survey, very similar for the two detectors, was carried out in two stages: the measurement of the positions of the modules on the ladders and the measurement of the positions of the ladder end points on the support cone.

In the first stage, for SDD for example [22], the three-dimensional positions of six reference markers engraved on the detector surface were measured for each module with respect to ruby reference spheres fixed to the support structure. The precision of the measuring machine was 5 μm in the coordinates on the ladder plane and about 10 μm in the direction orthogonal to the plane. The deviations of the reference marker coordinates on the plane with respect to design positions showed an average value of 1 μm and a r.m.s. of 20 μm. In the second stage, the positions of the ladder end points with respect to the cone support structure were measured with a precision of about 10 μm. However, for the outer SSD layer, the supports were dismounted and remounted after the survey; the precision of the remounting procedure is estimated to be around 20 μm in the $r\varphi$ direction [1].

In the following we describe the results for the validation of the SSD survey measurements with cosmic-ray data. The validation of the SDD survey will be performed after completion of the detector calibration.

5.1 Double points in SSD module overlaps

As already mentioned, the modules are mounted with a small (2 mm) overlap for both the longitudinal (z, modules on the same ladder) and transverse directions ($r\varphi$, adjacent ladders). These overlaps allow us to verify the relative position of neighbouring modules using double points produced by the same particle on the two modules. Since the two points are very close in space and the amount of material crossed by the particle between the two points is very limited, multiple scattering can be neglected.

We define the distance $\Delta x_{\rm loc}$ between the two points in the local x direction on the module plane ($\approx r\varphi$) by projecting, along the track direction, the point of one of the two modules on the other module plane. Figure 8 (left) shows the $\Delta x_{\rm loc}$ distribution with and without the survey corrections, for both SSD layers (it was verified that the distributions for the two layers are compatible [21, 23]) . When the survey corrections are applied, the spread of the distributions, obtained from a gaussian fit, is $\sigma \approx 25.5$ μm. This arises from the combined spread of the two points, thus the corresponding effective position resolution for a single point is estimated to be smaller by a factor $1/\sqrt{2}$, i.e. ≈ 18 μm, which is compatible with the expected intrinsic spatial resolution of about 20 μm. This indicates that the residual misalignment after applying the survey is negligible with respect to the intrinsic spatial resolution. This validation procedure was confirmed using Monte Carlo simulations of cosmic muons in the detector without misalignment, which give a spread in $\Delta x_{\rm loc}$ of about 25 μm, in agreement with that obtained from the data.

5.2 Track-to-point residuals in SSD

Another test that was performed uses two points in the outer SSD layer to define a straight track (no magnetic field) and inspects the residuals between points on the inner layer and the track. The residuals are calculated using the position along the track corresponding to the minimum of the weighted (dimensionless) distance to the point[2]. Figure 8 (right) shows the distribution of the $r\varphi$

[2]The different expected resolutions in $r\varphi$ and z have been taken into account in the calculation of the distance of closest approach by dividing the deviations by the expected uncertainties, i.e. making use of a dimensionless distance measure.

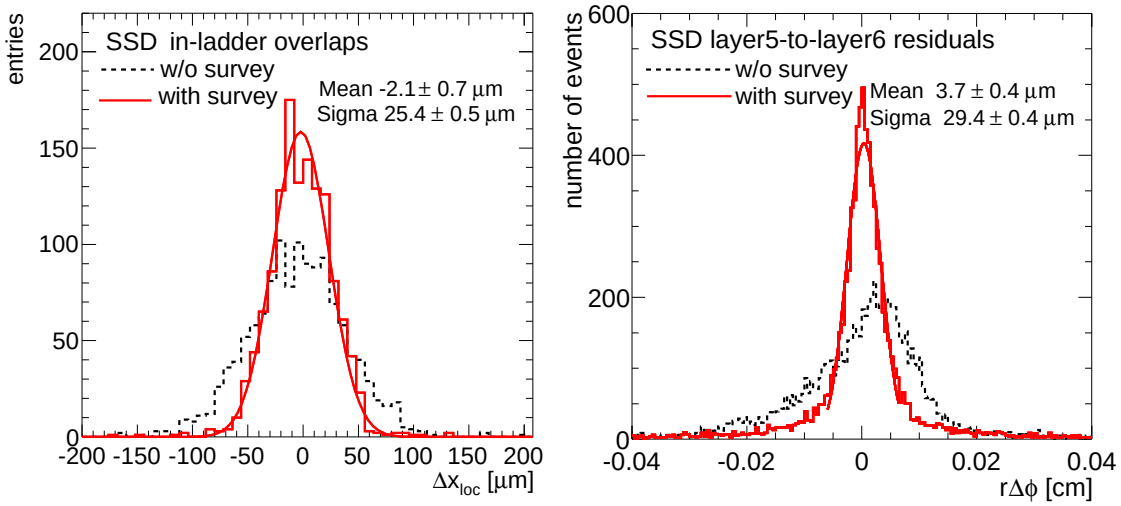

Figure 8. (colour online) SSD survey validation. Left: distribution of $\Delta x_{\rm loc}$, the distance between two points in the module overlap regions along z on the same ladder. Right: distribution of the $r\varphi$ residuals between straight-line tracks defined from two points on layer 6 and the corresponding points on layer 5. In both cases, gaussian fits to the distributions with survey applied are shown (in right-hand panel the fit range is $\pm 2\,\sigma$, i.e. $[-60\ \mu\text{m}, +60\ \mu\text{m}]$).

residuals between tracks through layer 6 and points on layer 5. The distribution exhibits significant non-gaussian tails, due to multiple scattering of low-momentum particles. The effect of multiple scattering on the residuals was analytically estimated to be of about 300 μm for $p = 0.5$ GeV/c and to be negligible for $p \gtrsim 7$ GeV/c. This is roughly compatible with the observed distribution of residuals. The width of the central part of the distribution is quantified by performing a gaussian fit truncated at $2\,\sigma$, that gives $\sigma_{r\varphi} = 29\ \mu$m. The spread contains a contribution from the uncertainty in the track trajectory due to the uncertainties in the points on the outer layer. Assuming the same resolution on the outer and inner layers and taking into account the geometry of the detector, the effective single point resolution spread is $1/\sqrt{1.902}$ times the overall spread [23], that is 21 μm. This spread is larger than the effective resolution of about 18 μm that is extracted from the double points in module overlaps. This difference could be partly due to the multiple scattering, relevant for this analysis and negligible for the overlaps analysis, but we can not rule out that additional misalignments with a r.m.s. up to about 15 μm are present in the SSD. The mean residual is also non-zero, $(3.7 \pm 0.4)\ \mu$m, which suggests that residual shifts at the 5–10 μm level could be present. These misalignments would have to be at the ladder level to be compatible with the result from the study with sensor module overlaps.

The same analysis was performed for the residuals in the z direction [21, 23], not shown here. The distributions without and with survey were found to be compatible and the corresponding effective single point resolution was found to be compatible with the expected intrinsic resolution of about 800 μm. This indicates that the residual misalignment in z is much smaller than the intrinsic SSD resolution.

A third method that was used to verify the SSD survey consisted in performing tracking with

pairs of points (2 points on layer 5 and two points on layer 6 or two sets of points on layer 5 and 6), and comparing the track parameters of both track segments. The conclusion from this method is consistent with the results from the track-to-point method. For details see [23].

6. ITS alignment with Millepede

In general, the task of the track-based alignment algorithms is determining the set of geometry parameters that minimize the global χ^2 of the track-to-point residuals:

$$\chi^2_{\text{global}} = \sum_{\text{modules, tracks}} \vec{\delta}^{\,\text{T}}_{t,p}\, \mathbf{V}^{-1}_{t,p}\, \vec{\delta}_{t,p}\,. \tag{6.1}$$

In this expression, the sum runs over all the detector modules and all the tracks in a given data set; $\vec{\delta}_{t,p} = \vec{r}_t - \vec{r}_p$ is the residual between the data point $\vec{r}_p$ and the reconstructed track extrapolation $\vec{r}_t$ to the module plane; $\mathbf{V}_{t,p}$ is the covariance matrix of the residual. Note that, in general, the reconstructed tracks themselves depend on the assumed geometry parameters. This section describes how this minimization problem is treated by Millepede [5, 24] —the main algorithm used for ITS alignment— and presents the first alignment results obtained with cosmic-ray data.

6.1 General principles of the Millepede algorithm

Millepede belongs to the *global least-squares minimization* type of algorithms, which aim at determining simultaneously all the parameters that minimize the global χ^2 in Eq. (6.1). It assumes that, for each of the local coordinates, the residual of a given track t to a specific measured point p can be represented in a linearized form as $\delta_{t,p} = \vec{a} \cdot \partial\delta_{t,p}/\partial\vec{a} + \vec{\alpha}_t \cdot \partial\delta_{t,p}/\partial\vec{\alpha}_t$, where $\vec{a}$ is the set of global parameters describing the alignment of the detector (three translations and three rotations per module) and $\vec{\alpha}_t$ is the set of local parameters of the track. The corresponding χ^2_{global} equation for n tracks with ν local parameters per track and for m modules with 6 global parameters ($N = 6m$ total global parameters) leads to a huge set of $N + \nu n$ normal equations. The idea behind the Millepede method is to consider the local $\vec{\alpha}$ parameters as nuisance parameters that are eliminated using the Banachiewicz identity [25] for partitioned matrices. This allows to build explicitly only the set of N normal equations for the global parameters. If needed, linear constraints on the global parameters can be added using the Lagrange multipliers. Historically, two versions, Millepede and Millepede II, were released. The first one was performing the calculation of the residuals, the derivatives and the final matrix elements as well as the extraction of the exact solution in one single step, keeping all necessary information in computer memory. The large memory and CPU time needed to extract the exact solution of a $N \times N$ matrix equation effectively limited its use to $N < 10,000$ global (alignment) parameters. This limitation was removed in the second version, Millepede II, which builds the matrices (optionally) in sparse format, to save memory space, and solves them using advanced iterative methods, much faster than the exact methods.

6.2 Millepede for the ALICE ITS

Following the development of Millepede, ALICE had its own implementation of both versions, hereafter indicated as MP and MPII, within the AliRoot framework [6]. Both consist of a detector independent solver class, responsible for building and solving the matrix equations, and a class

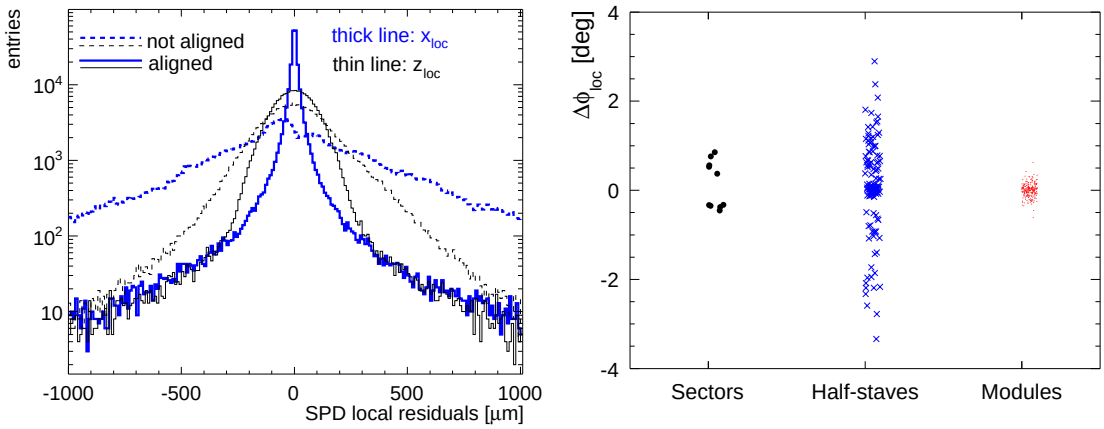

Figure 9. (colour online) Left: example of Millepede residuals in the local reference frame of the SPD modules before and after the alignment. Right: the corrections to the $\varphi_{\rm loc}$ angle obtained in the hierarchical SPD alignment with Millepede.

interfacing the former to specific detectors. While MP closely follows the original algorithm [5], MPII has a number of extensions. In addition to the MinRes matrix equation solution algorithm offered by the original Millepede II, the more general FGMRES [26] method was added, as well as the powerful ILU(k) matrix preconditioners [27]. All the results shown in this work are obtained with MPII.

The track-to-point residuals, used to construct the global χ^2, are calculated using a parametric straight line $\vec{r}(t) = \vec{a} + \vec{b}t$ or helix $\vec{r}(t) = \{a_x + r\cos(t+\varphi_0), a_y + r\sin(t+\varphi_0), a_z + b_z t\}$ track model, depending on the presence of the magnetic field. The full error matrix of the measured points is accounted for in the track fit, while multiple scattering is ignored, since it has no systematic effect on the residuals.

Special attention was paid to the possibility to account for the complex hierarchy of the alignable volumes of the ITS, in general leading to better description of the material budget distribution after alignment. This is achieved by defining explicit parent–daughter relationships between the volumes corresponding to mechanical degrees of freedom in the ITS. The alignment is performed simultaneously for the volumes on all levels of the hierarchy, e.g. for the SPD the corrections are obtained in a single step for the sectors, the half-staves within the sectors and the modules within the half-staves. Obviously, this leads to a degeneracy of the possible solutions, which should be removed by an appropriate set of constraints. We implemented the possibility to constrain either the mean or the median of the corrections for the daughter volumes of any parent volume. While the former can be applied via Lagrange multipliers directly at the minimization stage, the latter, being non-analytical, is applied after the Millepede minimization in a special post-processing step. The relative movement δ of volumes for which the survey data is available (e.g. SDD and SSD modules) can be restricted to be within the declared survey precision $\sigma_{\rm survey}$ by adding a set of gaussian constraints $\delta^2/\sigma^2_{\rm survey}$ to the global χ^2.

We report here two example figures to illustrate the bare output results from Millepede II for the alignment of the SPD detector (in this case), while the analysis of the alignment quality will be presented in the next section. The left-hand panel of Fig. 9 shows an example of the residuals in

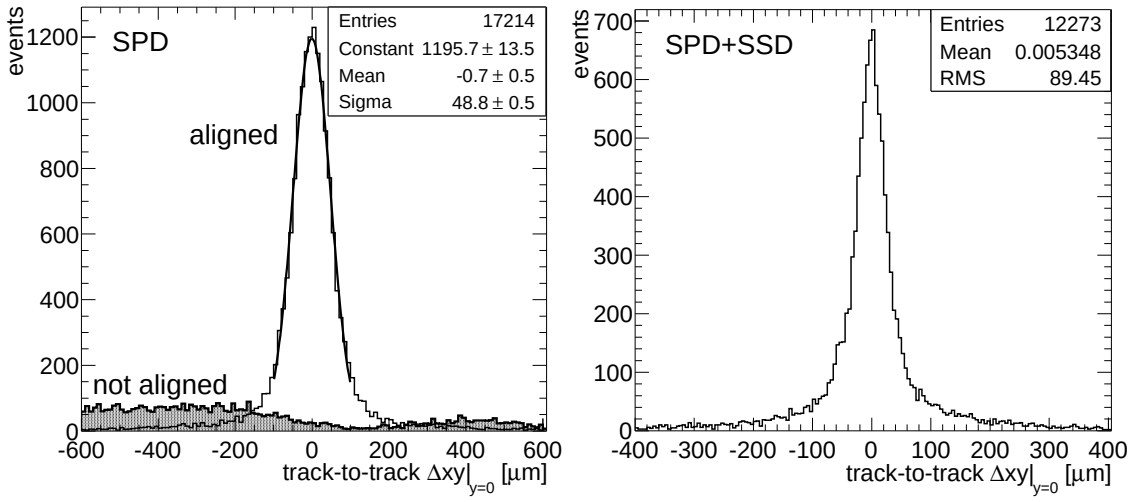

Figure 10. Left: distribution of $\Delta xy|_{y=0}$ for SPD only, before and after alignment. Right: distribution $\Delta xy|_{y=0}$ for track segments reconstructed in the upper and lower parts of SPD+SSD layers; each track segment is required to have four assigned points; SSD survey and Millepede alignment corrections are applied. In both cases, the distributions are produced from the sample of events used to obtain the alignment corrections.

SPD (in the local reference frame of the modules) before and after alignment. The right-hand panel of Fig. 9 shows the obtained corrections for the $\varphi_{\rm loc}$ angle (rotation of the volume with respect to its $z_{\rm loc}$ axis), indicating that the largest misalignments are at the level of the half-staves with respect to the carbon fiber support sectors.

6.3 Results on alignment quality

The SPD detector was first aligned using 5×10^4 cosmic-ray tracks, with two points in the inner layer and two points in the outer layer, collected in 2008 with the magnetic field switched off. As described in the previous section, the hierarchical alignment procedure consisted in: aligning the ten sectors with respect to each other, the twelve half-staves of each sector with respect to the sector, and the two modules of each half-stave with respect to the half-stave.

The following two observables are mainly used to check the quality of the obtained alignment: the top half-track to bottom half-track matching at the plane $y = 0$, and the track-to-point distance for the "extra" points in the acceptance overlaps.

For the first observable, the cosmic-ray track is split into the two track segments that cross the upper ($y > 0$) and lower ($y < 0$) halves of the ITS barrel, and the parameters of the two segments are compared at $y = 0$. The main variable is $\Delta xy|_{y=0}$, the track-to-track distance at $y = 0$ in the (x,y) plane transverse to beam line. This observable, that is accessible only with cosmic-ray tracks, provides a direct measurement of the resolution on the track transverse impact parameter d_0; namely: $\sigma_{\Delta xy|_{y=0}}(p_{\rm t}) = \sqrt{2}\,\sigma_{d_0}(p_{\rm t})$. Since the data used for the current analysis were collected without magnetic field, they do not allow us to directly assess the d_0 resolution (this will be the subject of a future work). However, also without a momentum measurement, $\Delta xy|_{y=0}$ is a powerful indicator of the alignment quality, as we show in the following.

Figure 10 (left) shows the distribution of $\Delta xy|_{y=0}$ for SPD, without and with the alignment

corrections. The two track segments are required to have a point in each of the SPD layers and to pass, in the transverse plane, within 1 cm from the origin (this cut selects tracks with a similar topology to those produced in collisions and rejects tracks that have small incidence angles on the inner layer modules). A gaussian fit to the distribution in the range $[-100\ \mu\mathrm{m}, +100\ \mu\mathrm{m}]$ gives a centroid compatible with zero and a spread $\sigma \approx 50\ \mu$m. For comparison, a spread of 38 μm is obtained from a Monte Carlo simulation, with the ideal geometry of the ITS (without misalignment), of cosmic muons generated according to the momentum spectrum measured by the ALICE TPC in cosmic runs with magnetic field. When only the SPD detector is used and the tracks are straight lines (no magnetic field), the spread of the $\Delta xy|_{y=0}$ distribution can be related in a simple way to the effective spatial resolution $\sigma_{\mathrm{spatial}}$, which includes the intrinsic sensor resolution and of the residual misalignment. For tracks passing close to the beam line (as in our case, with the cut at 1 cm), we have:

$$\sigma^2_{\Delta xy|_{y=0}} \approx 2\,\frac{(r^2_{\mathrm{SPD1}}\sigma^2_{\mathrm{spatial,SPD1}} + r^2_{\mathrm{SPD2}}\sigma^2_{\mathrm{spatial,SPD2}})}{(r_{\mathrm{SPD1}} - r_{\mathrm{SPD2}})^2} \approx 2\,\frac{r^2_{\mathrm{SPD1}} + r^2_{\mathrm{SPD2}}}{(r_{\mathrm{SPD1}} - r_{\mathrm{SPD2}})^2}\,\sigma^2_{\mathrm{spatial}}\,, \tag{6.2}$$

where the inner and outer SPD layers are indicated as SPD1 and SPD2, respectively. This relation neglects the effect of multiple scattering in the pixels and in the beam pipe, which is certainly one of the reasons why the $\Delta xy|_{y=0}$ distribution is not gaussian outside the central region, most likely populated by the high-momentum component of the cosmic muons. Using the fit result, $\sigma_{\Delta xy|_{y=0}} \approx 50\ \mu$m, obtained in the central region $[-100\ \mu\mathrm{m}, +100\ \mu\mathrm{m}]$, we estimate the value $\sigma_{\mathrm{spatial}} \approx 14\ \mu$m, not far from the intrinsic resolution of about 11 μm extracted from the simulation. However, a precise estimation of the effective spatial resolution with this method requires the measurement of the track momentum, to account properly for the multiple scattering contribution. The statistics collected in 2008 with magnetic field did not allow a momentum-differential analysis.

The next step in the alignment procedure is the inclusion of the SSD detector. As shown in section 5, the survey measurements already provide a very precise alignment, with residual misalignment levels of less than 5 μm for modules on the ladder and of about 20 μm for ladders. Because of the limited available statistics ($\approx 2 \times 10^4$ tracks with four points in SPD and four points in SSD), the expected level of alignment obtained with Millepede on single SSD modules is significantly worse than the level reached with the survey measurements. For this reason, Millepede was used only to align the whole SPD barrel with respect to the SSD barrel and to optimize the positioning of large sets of SSD modules, namely the upper and lower halves of layers 5 and 6. For this last step, the improvement on the global positioning of the SSD layers was verified by comparing the position and direction of the pairs of SSD-only track segments built using: two points in the upper and two in the lower half-barrel (upper–lower configuration) or two points in the inner and two in the outer layer (inner–outer configuration). Before the alignment (only the survey corrections applied), the mean of $\Delta xy|_{y=0}$ is $(120 \pm 7)\ \mu$m and $(-1.8 \pm 0.6)\ \mu$m for the upper–lower and inner–outer configurations, respectively. After the alignment, it is $(-5 \pm 6)\ \mu$m and $(0.5 \pm 0.6)\ \mu$m, respectively, that is, compatible with zero for both configurations.

The right-hand panel of Fig. 10 shows the distribution of $\Delta xy|_{y=0}$ for pairs of track segments, each reconstructed with two points in SPD and two in SSD, i.e. the merged cosmic-ray track has eight points in SPD+SSD. It can be seen that, when the SSD survey and the Millepede alignment are applied, the distribution is centred at zero and very narrow (FWHM $\approx 60\ \mu$m), but it shows

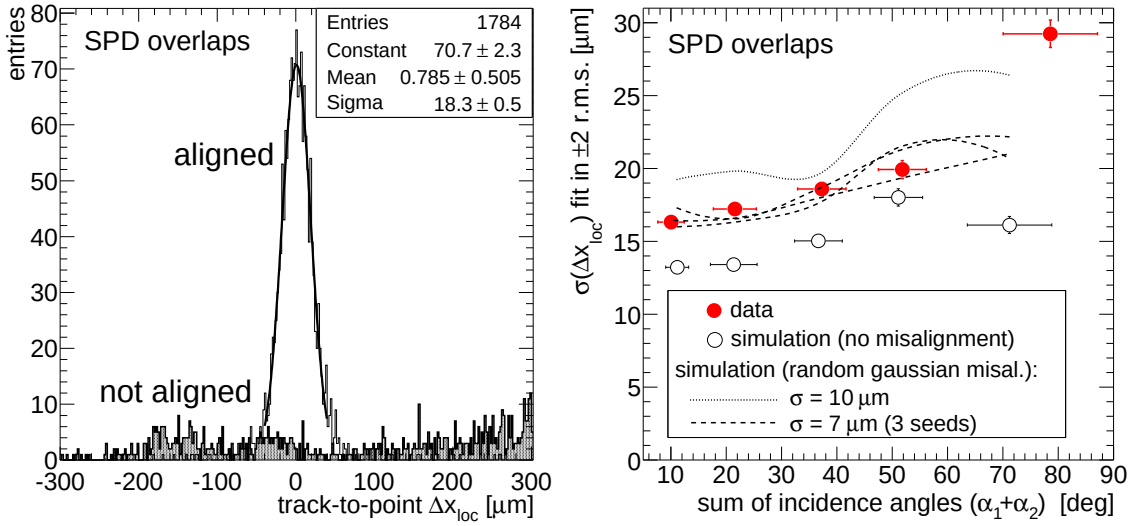

Figure 11. (colour online) SPD double points in acceptance overlaps. Left: track-to-point $\Delta x_{\rm loc}$ for "extra" points before and after alignment. Right: σ of the $\Delta x_{\rm loc}$ distributions as a function of the track-to-module incidence angle selection; 2008 cosmic-ray data are compared to the simulation with different levels of residual misalignment. See text for details.

non-gaussian tails, most likely due to multiple scattering. A more precise alignment of the SSD using high-momentum tracks will be performed with the 2009 cosmic-ray and proton–proton data.

The second alignment quality observable is the $\Delta x_{\rm loc}$ distance between points in the region where there is an acceptance overlap between two modules of the same layer. Because of the short radial distance between the two overlapping modules (a few mm), the effect of multiple scattering is negligible. However, in order to relate the spread of $\Delta x_{\rm loc}$ to the effective resolution, the dependence of the intrinsic sensor resolution on the track-to-module incidence angle has to be accounted for. In particular, for SPD, due to the geometrical layout of the detector (Fig. 3, left), the track-to-module incidence angles in the transverse plane are in general not equal to 90° and they are very different for two adjacent overlapping modules crossed by the same track. If $\Delta x_{\rm loc}$ is defined as described in section 5, the error on $\Delta x_{\rm loc}$ can be related to the effective spatial resolution of the two points, $\sigma_{\rm spatial}$, as:

$$\sigma^2_{\Delta x_{\rm loc}} = \sigma^2_{\rm spatial}(\alpha_2) + \sigma^2_{\rm spatial}(\alpha_1)\cos^2(\varphi_{12}) \tag{6.3}$$

where the 1 and 2 subscripts indicate the two overlapping points, α_i is the incidence angle of the track on the module plane, and φ_{12} is the relative angle between the two module planes, which is 18° and 9° on the inner and outer SPD layer, respectively. Note that, for SSD overlaps on the same ladder, we have $\alpha_1 = \alpha_2 \simeq 90°$ and $\varphi_{12} = 0$; therefore, $\sigma_{\Delta x_{\rm loc}} = \sqrt{2}\,\sigma_{\rm spatial}$, which is the relation we used in section 5.

We start by showing, in Fig. 11 (left), the track-to-point distance $\Delta x_{\rm loc}$ for the SPD "extra" points in the transverse plane, before and after the Millepede alignment. The extra points are not used in the alignment procedure. The spread of the distribution is $\sigma \approx 18\ \mu$m, to be compared to $\sigma \approx 15\ \mu$m from a Monte Carlo simulation with ideal geometry. An analysis of the $\Delta x_{\rm loc}$ distance as a function of the α incidence angle has been performed: five windows on the sum $(\alpha_1 + \alpha_2)$

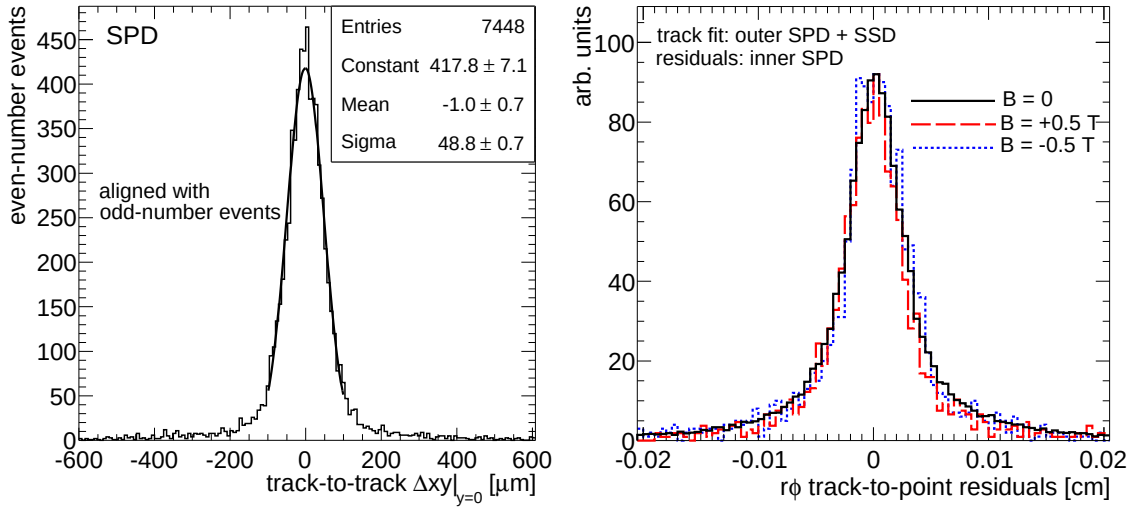

Figure 12. (colour online) Alignment stability tests. Left: for SPD only, distribution of the $\Delta xy|_{y=0}$ distance obtained when aligning with every second track and checking the alignment with the other tracks. Right: track-to-point residuals in the inner SPD layer (track fit in outer SPD layer and in the two SSD layers), for B = 0 and B = ±0.5 T (the three histograms are normalized to the same integral).

of the incidence angles on the two overlapping modules have been considered. These windows define increasing ranges of incidence angles from 0° to 50°. Figure 11 (right) shows the spread of the $\Delta x_{\rm loc}$ distribution for the different incidence angle selections: a clear dependence of the spread (hence of the spatial resolution) on the incidence angle can be seen. This dependence was already observed in SPD test beam measurements [28, 29], which were used to tune the detector response simulation in the AliRoot software. In the same figure, Monte Carlo simulation results are reported for comparison: simulation with ideal geometry (open circles) and with a misaligned geometry obtained using a random gaussian residual misalignment (dashed lines: misalignments with $\sigma = 7$ μm and three different seeds; dotted line: misalignments with $\sigma = 10$ μm). The 2008 data are well described by the simulation with a random residual misalignment with $\sigma \approx 7$ μm. However, this conclusion is based on the assumption that the intrinsic resolution is the same in the real detector and in the simulation. Since the intrinsic resolution can slightly vary depending on the working conditions of the detector (e.g. the settings used for the bias voltage and for the threshold), the value of 7 μm for the residual misalignment should be taken only as an indication. Furthermore, this is an equivalent random misalignment, while the real misalignments are likely non-gaussian and to some extent correlated among different modules.

The robustness of the obtained results was tested by dividing the data sample in two parts and using every second track to align the SPD and the others to check the alignment quality. The corresponding $\Delta xy|_{y=0}$ distribution is presented in the left-hand panel of Fig. 12: the distribution is centred at zero and has the same $\sigma \approx 50$ μm as in the case of aligning with all tracks.

Finally, the data with the 0.5 T magnetic field switched on (a few thousand events collected at the end of the 2008 cosmic run) were used to perform dedicated checks to evaluate a possible effect of the field on the alignment. The alignment corrections extracted from data with B = 0 were

applied to data with B $= \pm 0.5$ T and alignment quality was verified using both the extra points method and the track-to-point residuals method. The distributions of the track-to-point distance for extra points in SPD acceptance overlaps for B $= 0$, $+0.5$ T and -0.5 T data were found to have compatible widths (σ [μm]: 18.3 ± 0.5, 17.8 ± 2.3, 18.4 ± 1.8, respectively) [21]. Another check was performed using the track-to-point residuals, calculated by fitting the tracks in the SSD layers and the outer SPD layer and evaluating the residuals in the inner SPD layer. In Fig. 12 (right) the comparison between the residuals without magnetic field, with $+0.5$ T, and with -0.5 T is shown. Also in this case, the distributions without field and with the two field polarities are compatible.

6.4 Prospects for inclusion of SDD in the Millepede procedure

The alignment of the SDD detectors for the $x_{\rm loc}$ coordinate (reconstructed from the drift time) is complicated by the interplay between the geometrical misalignment and the calibration of drift velocity and t_0 (defined in section 2.2). The t_0 parameter accounts for the delays between the time when a particle crosses the detector and the time when the front-end chips receive the trigger signal. Two methods have been developed in order to obtain a first estimate of the t_0 parameter. The first, and simpler, method consists in extracting the t_0 from the minimum measured drift time on a large statistics of reconstructed SDD points. The sharp rising part of the distribution of measured drift times is fitted with an error function. The t_0 value is then calculated from the fit parameters. The second method measures the t_0 from the distributions of residuals along the drift direction ($x_{\rm loc}$) between tracks fitted in SPD and SSD layers and the corresponding points reconstructed in the SDD. These distributions, in case of miscalibrated t_0, show two opposite-signed peaks corresponding to the two separated drift regions of each SDD module, where electrons move in opposite directions (see Fig. 4, right). The t_0 can be calculated from the distance of the two peaks and the drift velocity. This second procedure has the advantage of requiring smaller statistics, because it profits from all the reconstructed tracks, with the drawback of relying on SDD calibration parameters (the drift velocity and possibly the correction maps). Moreover, being based on track reconstruction, it might be biased by SPD and/or SSD misalignments.

Depending on the available statistics, the t_0 determination with these two methods can be done at the level of SDD barrel, SDD ladders or SDD modules. The t_0 parameter needs actually to be calibrated individually for each of the 260 SDD modules, because of differences in the overall length of the cables connecting the DAQ cards and the front-end electronics. In particular, a significant difference is expected between modules of the A ($z > 0$) and C sides ($z < 0$), due to the ≈ 6 m difference in the length of the optical fibres connecting the ITS ladders to the DAQ cards. With the first 2000 tracks, it is possible to determine the t_0 from track-to-point residuals for 4 sub-samples of modules, i.e. separating sensors connected to sides A and C of layers 3 and 4. An example of residual distributions for the left and right drift sides of the modules of layer 4 side C is shown in Fig. 13. The Millepede alignment corrections for SPD and SSD are applied in this case, and it has been checked that, if they are not applied, the centroid positions in this figure are not affected significantly, while the spread of the distributions increases, as it could be expected. A difference of 25 ns between sides A and C of each SDD layer has been observed, in agreement with the 6 m difference in fibre lengths (the propagation time of light in optical fibres is 4.89 ns/m). With larger statistics (35,000 tracks), it is possible to extract the t_0 for each half-ladder, which requires producing 36(ladders)$\times$2(A/C sides) pairs of histograms like the ones shown in Fig. 13 (left). Further

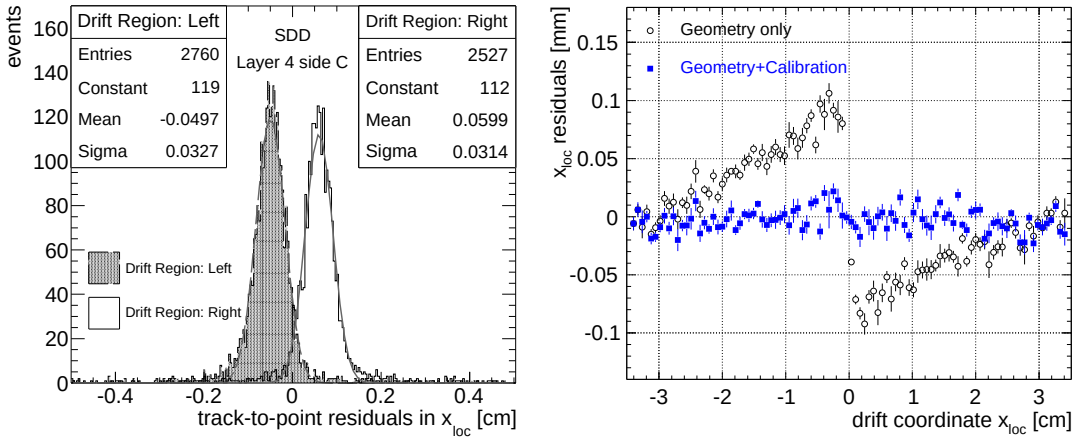

Figure 13. SDD calibration and alignment. Left: distribution of track-to-point residuals in the two drift regions for the SDD modules of layer 4 side C ($z < 0$); tracks are fitted using only their associated points in SPD and SSD; the Millepede alignment corrections for SPD and SSD are included, as well as the SSD survey. Right: residuals along the drift coordinate for one SDD module as a function of drift coordinate after Millepede alignment with only geometrical parameters and with geometrical+calibration parameters.

cable-length differences, which introduce t_0 difference, exist at the level of individual half ladders and at the level of individual modules. These differences are of the order of 1.5 m (7 ns) and 20 cm (< 1 ns) respectively, but have not been measured in detail yet, because of the limited size and coverage of the cosmic-ray tracks data sample. It should be noted that given the ≈ 6.5 μm/ns of drift velocity, a bias of 1 ns on the t_0 can lead to a significant effect on the reconstructed position along the drift coordinate $x_{\rm loc}$.

After a first calibration with these methods, a refinement of the t_0 determination is obtained by running the Millepede minimization with the t_0 as a free global parameter for each of the 260 SDD modules. Similarly, the drift velocity is considered as a free parameter for those SDD modules (about 35%) with mal-functioning injectors. For these modules a single value of drift velocity is extracted for the full data sample analyzed, thus neglecting the possible dependence of drift velocity on time due to temperature instabilities. However, this is not a major concern since the drift velocity was observed to be remarkably stable during the data taking [17]. This allows to assess at the same time geometrical alignment and calibration parameters of the SDD detectors. About 500 tracks are required to align and calibrate a single SDD module. An example is shown for a specific SDD module in the right-hand panel of Fig. 13, where the $x_{\rm loc}$ residuals along the drift direction are shown as a function of $x_{\rm loc}$. The result obtained using only the geometrical rotations and translations as free parameters in the Millepede minimization is shown by the circle markers. The clear systematic shift between the two drift regions ($x_{\rm loc} < 0$ and $x_{\rm loc} > 0$) is due to both miscalibrated t_0 and biased drift velocity (this is a module with non-working injectors). These systematic effects are no longer present when also the calibration parameters are fitted by Millepede (square markers). It should be pointed out that the width of the SDD residual distributions shown in Fig. 13 does not correspond to the expected resolution on SDD points along drift coordinate because of jitter between the time when the muon crosses the detectors and the SPD FastOR trigger, which has an integration time of 100 ns. For the about 100 SDD modules with highest occupancy,

the statistics collected in the 2008 cosmic run allowed to check the reliability of the calibration parameters (t_0 and drift velocity) extracted with Millepede by comparing the values obtained from independent analyses of two sub-samples of tracks. From this study, a precision of 0.025 μm/ns for the drift velocity and 10 ns for t_0 was estimated. It should be noted that these precisions are limited by the available statistics as well as by the trigger jitter effect mentioned above.

7. SPD alignment with an iterative local method

We developed an alignment method that performs a (local) minimization for each single module and accounts for correlations between modules by iterating the procedure until convergence is reached. A similar approach is considered by both the CMS and ATLAS experiments [30–32]. The main difference between this method and the Millepede algorithm is that only in the latter the correlations between the alignment parameters of all modules are explicitly taken into account. Conversely, the local module-by-module algorithm assumes that the misalignments of the modules crossed by a given track are uncorrelated and performs the minimization of the residuals independently for each module. The comparison of the alignment parameters from this method and from Millepede would provide a further validation of the results achieved with the Millepede.

In the local method we minimize, module-by-module, the following local χ^2 function of the alignment parameters of a single module:

$$\begin{aligned}\chi^2_{\text{local}}(\vec{a}_{\text{tra}}, \mathbf{A}_{\text{rot}}) &= \sum_{\text{tracks}} \vec{\delta}^{\,\text{T}}_{t,p}\, \mathbf{V}^{-1}_{t,p}\, \vec{\delta}_{t,p} \\ &= \sum_{\text{tracks}} \left(\vec{r}_t - \mathbf{A}_{\text{rot}}\vec{r}_p - \vec{a}_{\text{tra}}\right)^{\text{T}} \left(\mathbf{V}_t + \mathbf{V}_p\right)^{-1} \left(\vec{r}_t - \mathbf{A}_{\text{rot}}\vec{r}_p - \vec{a}_{\text{tra}}\right) . \end{aligned} \tag{7.1}$$

Here, the sum runs over the tracks passing through the module, $\vec{r}_p$ is the position of the measured point on the module while $\vec{r}_t$ is the crossing point on the module plane of the track t fitted with all points but $\vec{r}_p$. $\mathbf{V}_t$ and $\mathbf{V}_p$ are the covariance matrices of the crossing point and of the measured point, respectively. The six alignment parameters enter this formula in the vector $\vec{a}_{\text{tra}}$, the alignment correction for the position of the centre of the module, and in the rotation matrix $\mathbf{A}_{\text{rot}}$, the alignment correction for the orientation of the plane of the module. The alignment correction is supposed to be small so that the rotation matrix can be approximated as the unity matrix plus a matrix linear in the angles. In this way, the χ^2_{local} is a quadratic expression of the alignment parameters and the minimization can be performed by simple inversion. The χ^2_{local} function in Eq. (7.1) can be written in the same way also for a set of modules considered as a rigid block. The track parameters are not affected by the misalignment of the module under study, because the track point on this module is not used in the fit, while the positions of the crossing points are affected, because the tracks are propagated to the plane of the module defined in the ideal geometry. This is taken into account by adding a large error along the track direction to the covariance matrix of the crossing point.

Given that this is a local method, it is expected to work best if two conditions are fulfilled: the correlation between the misalignments of different modules is small and the tracks used to align a given module cross several other modules. In order to limit the bias that can be introduced by modules with low statistics, for which the second condition is normally not met, we align the modules following a sequence of decreasing number of points. To reduce the residual correlation

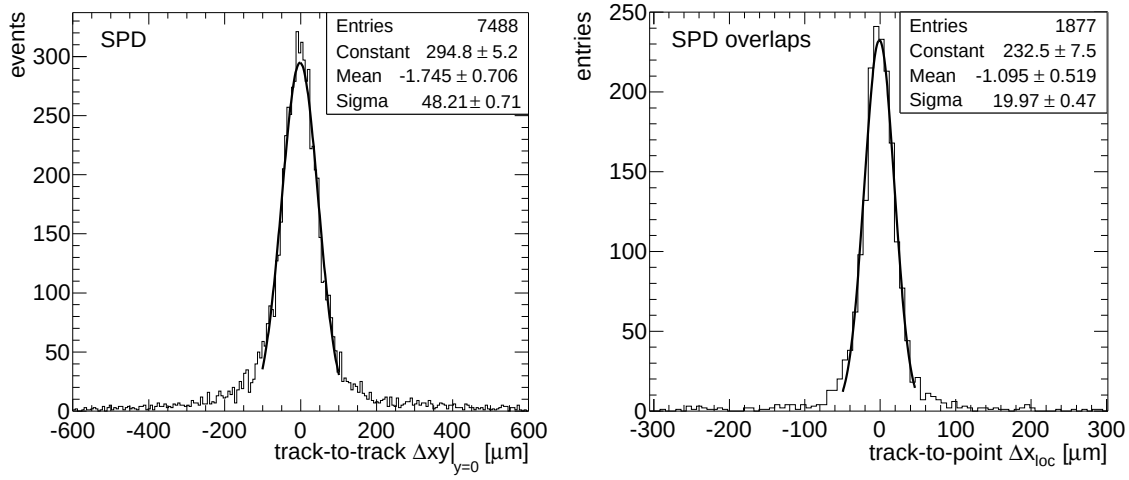

Figure 14. SPD alignment quality results for the iterative local method. Left: track-to-track $\Delta xy|_{y=0}$ distribution defined in section 6.3, using only SPD points. Right: track-to-point $\Delta x_{\rm loc}$ distribution for extra points in acceptance overlaps.

between the alignment parameters obtained for the different modules, we iterate the procedure until the parameters converge. Simulation studies with misalignments of the order of 100 μm have shown that the convergence is reached after about 10 iterations.

For the ITS alignment using the 2008 cosmic-ray data, we aligned only the SPD modules using this method. Like for Millepede, we adopted a hierarchical approach. Given the excellent precision of the SSD survey measurements, we used these two layers as a reference. We aligned as a first step the whole SPD barrel with respect to the SSD, then the two half-barrels with respect to the SSD, then the SPD sectors with respect to the SSD. In the last step, we used SPD and SSD points to fit the tracks and we aligned the individual sensor modules of the SPD. Figure 14 shows the top–bottom track-to-track $\Delta xy|_{y=0}$ distribution obtained using only the SPD points (left-hand panel) and the track-to-point $\Delta x_{\rm loc}$ for the double points in acceptance overlaps (right-hand panel), after alignment. Both distributions are compatible (mean and sigma from a gaussian fit) with the corresponding distributions after Millepede alignment. This is an important independent verification of the Millepede results. Since the two methods are in many aspects independent, comparing the two sets of alignment parameters could provide a check for the presence of possible systematic trends. Figure 15 shows the correlation of the inner SPD layer parameter values obtained with the iterative method and those obtained with Millepede. A correction was applied to account for a possible global roto-translation of the whole ITS, which does not affect the quality of the alignment and can be different for the two methods. The closed (open) markers represent the modules with more (less) than 500 track points. Most of the modules are clustered along the diagonal lines where the parameters from the two methods are exactly the same. There are some outlier modules, that are far from the ideal result. However, these outliers mostly correspond to modules with low statistics (open markers) at the sides of the SPD barrel.

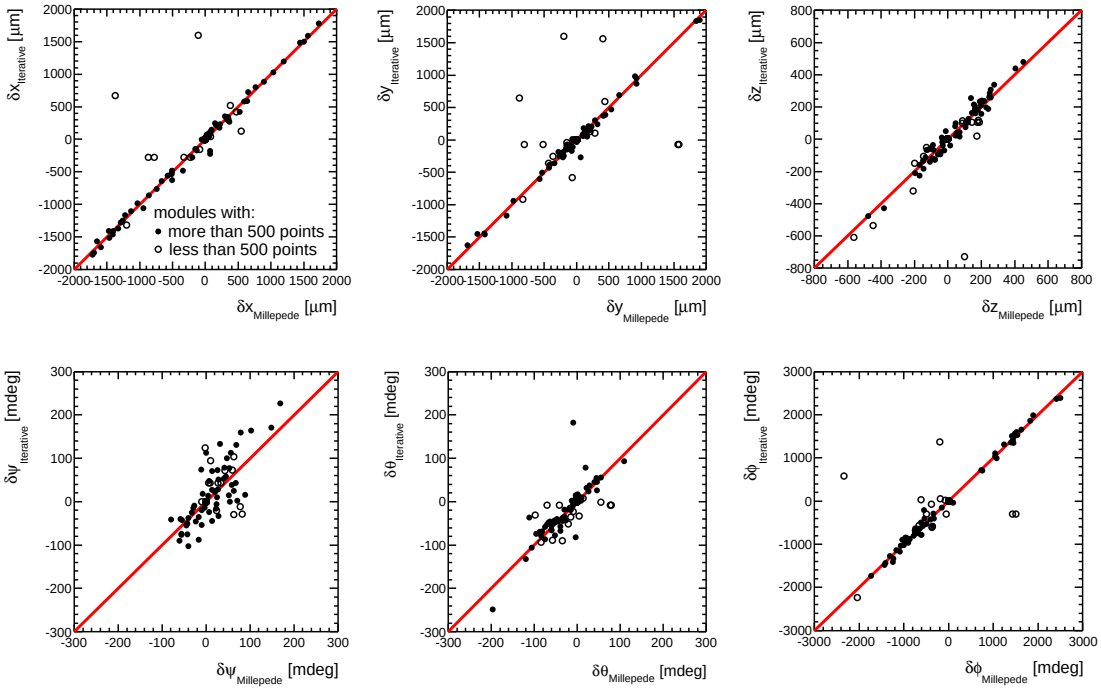

Figure 15. Correlation between the alignment parameters obtained from Millepede (horizontal axis) and the iterative method (vertical axis), for the inner SPD layer modules. Modules with more (less) than 500 points are represented by the closed (open) markers.

8. Conclusions

The results on the first alignment of the ALICE Inner Tracking System with cosmic-ray tracks, collected in 2008 in the absence of magnetic field, have been presented.

The initial step of the alignment procedure consisted of the validation of the survey measurements for the Silicon Strip Detector (SSD). The three methods applied for this purpose indicate that the residual misalignment spread for modules on ladders is less than 5 μm, i.e. negligible with respect to the intrinsic resolution of this detector in the most precise direction, while the residual misalignment spread for the ladders with respect to the support cones amounts to about 15 μm.

The procedure continues with track-based software alignment performing residuals minimization. We presented the results obtained with a sample of about 10^5 cosmic-ray tracks, reconstructed in events selected by the FastOR trigger of the Silicon Pixel Detector (SPD). We mainly use the Millepede algorithm, which minimizes a global χ^2 of residuals for all alignable volumes and a large set of tracks.

We start from the SPD, which is aligned in a hierarchical approach, from the largest mechanical structures (10 support sectors) to the 240 single sensor modules. About 90% of the latter were active during the 2008 cosmic run, and about 85% had enough space points (> 50) to perform alignment. Then, we align the SPD barrel with respect to the SSD barrel. The SSD coverage provided by the cosmic-ray tracks is insufficient to align the SSD at the level of ladders, especially for the ladders

close to the horizontal plane $y = 0$. Therefore, for the time being we only align the SSD at the level of large sets of ladders.

The two intermediate ITS layers, the Silicon Drift Detectors (SDD), represent a special case, because the reconstruction of one of the two local coordinates requires dedicated calibration procedures (drift velocity and drift time zero extraction), which are closely related to the alignment. Indeed, one of the approaches that we are developing for the time zero calibration is based on the analysis of track residuals in a standalone procedure, initially, and then directly within the Millepede algorithm. Once these procedures are stable and robust, the SDD will be included in the standard alignment chain. For all six layers, the completion of the alignment for all modules will require tracks from proton–proton collisions; a few 10^6 events (collected in a few days) should allow us to reach a uniform alignment level, close to the target, over the entire detector.

We use mainly two observables to assess the quality of the obtained alignment: the matching of the two half-tracks produced by a cosmic-ray particle in the upper and lower halves of the ITS barrel, and the residuals between double points produced in the geometrical overlaps between adjacent modules. For the SPD, both observables indicate an effective space point resolution of about 14 μm in the most precise direction, only 25% worse than the resolution of about 11 μm extracted from the Monte Carlo simulation without misalignments. In addition, the measured incidence angle dependence of the spread of the double points residuals is well reproduced by Monte Carlo simulations that include random residual misalignments with a gaussian sigma of about 7 μm. Further confidence on the robustness of the results is provided, to some extent, by the cross-checks we performed using a small data set with magnetic field switched on and, mainly, by the comparison of the Millepede results to those from a second, independent, alignment method. This second method, which iteratively minimizes a set of local module-by-module χ^2 functions, yields, compared to Millepede, a similar alignment quality and a quite compatible set of alignment corrections.

Using the present data set with magnetic field off, since the track momenta are not known, the multiple scattering effect, which is certainly not negligible, cannot be disentangled from the residual misalignment effect. Therefore, a more conclusive statement on the SPD residual misalignment will be possible only after the analysis of cosmic-ray data collected with magnetic field switched on. The same applies for combined tracking with SPD, SDD and SSD points: in this case, the momentum-differential analysis of the transverse distance between the two half-tracks (upper and lower half-barrels) will allow us to measure the track transverse impact parameter resolution, which is a key performance figure in view of the ALICE heavy flavour physics program.

Acknowledgements

The ALICE collaboration would like to thank all its engineers and technicians for their invaluable contributions to the construction of the experiment, and, in particular, of the Inner Tracking System.

The ALICE collaboration acknowledges the following funding agencies for their support in building and running the ALICE detector:

- Calouste Gulbenkian Foundation from Lisbon and Swiss Fonds Kidagan, Armenia;

- Conselho Nacional de Desenvolvimento CientŠfico e TecnolŮgico (CNPq), Financiadora de Estudos e Projeto (FINEP), Fundação de Amparo à Pesquisa do Estado de São Paulo (FAPESP);
- National Natural Science Foundation of China (NSFC), the Chinese Ministry of Education (CMOE) and the Ministry of Science and Technology of China (MSTC);
- Ministry of Education and Youth of the Czech Rebublic;
- Danish National Science Research Council and the Carlsberg Foundation;
- The European Research Council under the European Community's Seventh Framework Programme;
- Helsinki Institute of Physics and the Academy of Finland;
- French CNRS-IN2P3, the 'Region Pays de Loire', 'Region Alsace', 'Region Auvergne' and CEA, France;
- German BMBF and the Helmholtz Association;
- Hungarian OTKA and National Office for Research and Technology (NKTH);
- Department of Atomic Energy and Department of Science and Technology of the Government of India;
- Istituto Nazionale di Fisica Nucleare (INFN) of Italy;
- MEXT Grant-in-Aid for Specially Promoted Research, Japan;
- Joint Institute for Nuclear Research, Dubna;
- Korea Foundation for International Cooperation of Science and Technology (KICOS);
- CONACYT, DGAPA, México, ALFA-EC and the HELEN Program (High-Energy physics Latin-American–European Network);
- Stichting voor Fundamenteel Onderzoek der Materie (FOM) and the Nederlandse Organistie voor Wetenschappelijk Onderzoek (NWO), Netherlands;
- Research Council of Norway (NFR);
- Polish Ministry of Science and Higher Education;
- National Authority for Scientific Research - NASR (Autontatea Nationala pentru Cercetare Stiintifica - ANCS);
- Federal Agency of Science of the Ministry of Education and Science of Russian Federation, International Science and Technology Center, Russian Federal Agency of Atomic Energy, Russian Federal Agency for Science and Innovations and CERN-INTAS;

- Ministry of Education of Slovakia;
- CIEMAT, EELA, Ministerio de Educación y Ciencia of Spain, Xunta de Galicia (Consellería de Educación), CEADEN, Cubaenergía, Cuba, and IAEA (International Atomic Energy Agency);
- Swedish Reseach Council (VR) and Knut & Alice Wallenberg Foundation (KAW);
- Ukraine Ministry of Education and Science;
- United Kingdom Science and Technology Facilities Council (STFC);
- The United States Department of Energy, the United States National Science Foundation, the State of Texas, and the State of Ohio.

References

[1] K. Aamodt et al. [ALICE Collaboration], *JINST* **3** (2008) S08002.

[2] F. Carminati et al. [ALICE Collaboration], *J. Phys. G* **30** (2004) 1517, chapter 1 and references therein.

[3] U. Heinz and M. Jacob, arXiv:nucl-th/0002042, and references therein;
I. Arsene et al. [BRAHMS Collaboration], *Nucl. Phys. A* **757** (2005) 1;
K. Adkox et al. [PHENIX Collaboration], *Nucl. Phys. A* **757** (2005) 184;
B.B. Back et al. [PHOBOS Collaboration], *Nucl. Phys. A* **757** (2005) 28;
J. Adams et al. [STAR Collaboration], *Nucl. Phys. A* **757** (2005) 102.

[4] B. Alessandro et al. [ALICE Collaboration], *J. Phys. G* **32** (2006) 1295.

[5] V. Blobel and C. Kleinwort, contribution to the *Conference on Advanced Statistical Techniques in Particle Physics*, Durham, March, 18–22, 2002.

[6] ALICE Off-line framework, AliRoot, http://aliceinfo.cern.ch/Offline

[7] R. Brun and F. Rademakers, *Nucl. Inst. and Meth. A* **389** (1997) 81. See also http://root.cern.ch/.

[8] S. Beole et al., *Nucl. Inst. and Meth. A* **582** (2007) 733.

[9] G. Giraudo et al., *JINST* 4 (2009) P01003.

[10] A. Rashevsky et al., *Nucl. Inst. and Meth. A* **572** (2007) 125.

[11] G. Batigne et al., *JINST* 3 (2008) P06004.

[12] F. Agnese et al., *Nucl. Inst. and Meth. A* **562** (2006) 110.

[13] J. Alison [ATLAS Collaboration], ATL-INDET-PROC-2009-004 in *Proceedings of ACAT 2008*, Erice (Italy), November 3-7, 2008.

[14] S. Blusk et al., *Proceedings of the first LHC detector alignment workshop*, CERN, September 4–6, 2006, CERN-2007-004.

[15] B.S. Nilsen et al., *Nucl. Inst. and Meth. A* **599** (2009) 176.

[16] R. Santoro et al., *JINST* 4 (2009) P03023.

[17] B. Alessandro et al., arXiv:1001.3088, submitted to *JINST*.

[18] G.J.L. Nooren, to appear as PoS(RD09)009.

[19] K. Aamodt et al. [ALICE Collaboration], *Eur. Phys. J. C* **65** (2010) 111.

[20] E. Crescio et al., ALICE Internal Note 2009-046 (2009).

[21] C. Bombonati et al., ALICE Internal Note 2009-035 (2009).

[22] B. Alessandro et al., ALICE Internal Note 2009-047 (2009).

[23] A. Dainese et al., ALICE Internal Note 2009-045 (2009).

[24] V. Blobel, in *Proceedings of the first LHC detector alignment workshop*, CERN, September 4–6, 2006, CERN-2007-004.

[25] R.A. Frazer, W.J. Duncan and A.R. Collar, *Elementary Matrices and Some Applications to Dynamics and Differential Equations*, Cambridge University Press, Cambridge (1938).

[26] Y. Saad and M.H. Schultz, *SIAM J. Sci. Stat. Comput.* 7 (1986) 856.

[27] I.S. Duff, A.M. Erisman and J.K. Reid, *Direct methods for sparse matrices*, Oxford University Press, London (1986).

[28] G.E. Bruno et al., ALICE Internal Note 2005-011 (2005).

[29] G.E. Bruno et al., ALICE Internal Note 2005-022 (2005).

[30] P. Brückman de Renstrom, in *Proceedings of the first LHC detector alignment workshop*, CERN, September 4–6, 2006, CERN-2007-004.

[31] F.-P. Schilling, in *Proceedings of the first LHC detector alignment workshop*, CERN, September 4–6, 2006, CERN-2007-004.

[32] V. Karimaki et al., CMS Note 2006/008 (2006).